SARS-CoV-2 infects brain astrocytes of COVID-19 patients and impairs neuronal viability

Fernanda Crunfli[1#], Victor Corasolla Carregari[1#], Flavio Protasio Veras[2,3#], Pedro Henrique Vendramini[1], Aline Gazzola Fragnani Valença[1], André Saraiva Leão Marcelo Antunes[1], Caroline Brandão-Teles[1], Giuliana da Silva Zuccoli[1], Guilherme Reis-de-Oliveira[1], Lícia C. Silva-Costa[1], Verônica Monteiro Saia-Cereda[1], Bradley Joseph Smith[1], Ana Campos Codo[4], Gabriela Fabiano de Souza[5], Stéfanie Primon Muraro[5] , Pierina Lorencini Parise[5], Daniel A. Toledo-Teixeira[5], Ícaro Maia Santos de Castro[2], Bruno Marcel Silva Melo[2,3], Glaucia M. Almeida[6], Egidi Mayara Silva Firmino[3], Isadora Marques Paiva[2,3], Bruna Manuella Souza Silva[2,3], Rafaela Mano Guimarães[2,3], Niele D. Mendes[6], Raíssa Guimarães Ludwig[7], Gabriel Palermo Ruiz[7], Thiago Leite Knittel[7], Gustavo Gastão Davanzo[4], Jaqueline Aline Gerhardt[7], Patrícia Brito Rodrigues[8], Julia Forato[5], Mariene Ribeiro Amorim[5], Natália Brunetti Silva[9], Matheus Cavalheiro Martini[5], Maíra Nilson Benatti[10], Sabrina Batah[10], Li Siyuan[10], Rafael Batista João[11], Lucas Scardua Silva[11], Mateus Henrique Nogueira[11], Ítalo Karmann Aventurato[11], Mariana Rabelo de Brito[11] , Marina Koutsodontis Machado Alvim[11], José Roberto da Silva Júnior[12], Lívia Liviane Damião[12], Maria Ercilia de Paula Castilho Stefano[12], Iêda Maria Pereira de Sousa[12], Elessandra Dias da Rocha[12], Solange Maria Gonçalves[12], Luiz Henrique Lopes da Silva[12], Vanessa Bettini[12], Brunno Machado de Campos[11], Guilherme Ludwig[13], Lucas Alves Tavares[14,15], Marjorie Cornejo Pontelli[14,15], Rosa Maria Mendes Viana[14,15], Ronaldo Martins[14,15], Andre S. Vieira[16], José Carlos Alves-Filho[2,3], Eurico Arruda[14,15], Guilherme Podolski-Gondim[17], Marcelo Volpon Santos[17], Luciano Neder[17], Fernando Cendes[11], Paulo Louzada-Junior[2], Renê Donizeti Oliveira[2], Fernando Queiroz Cunha[2,3], André Damásio[7,18], Marco Aurélio Ramirez Vinolo[8,18,19] Carolina Demarchi Munhoz[20], Stevens K. Rehen[21,22], Helder I Nakaya[2,23], Thais Mauad[24], Amaro Nunes Duarte-Neto[24], Luiz Fernando Ferraz da Silva[24], Marisa Dolhnikoff [24], Paulo Saldiva[24], Alessandro S. Farias[9,18,19], Pedro Manoel M. Moraes-Vieira[4,18,19], Alexandre Todorovic Fabro[10], Adriano S. Sebollela[6], José Luiz Proença Módena[5], **Clarissa Lin Yasuda[11*], Marcelo A. Mori[7,18,19*], Thiago Mattar Cunha[2,3*], Daniel Martins-de-Souza[1,18,25,26,*].**

1- Laboratory of Neuroproteomics, Department of Biochemistry and Tissue Biology, Institute of Biology, University of Campinas (UNICAMP), Campinas, São Paulo, Brazil;

2- Center for Research in Inflammatory Diseases (CRID), Ribeirão Preto Medical School (FMRP), University of São Paulo (USP), Ribeirão Preto, São Paulo, Brazil;

3- Department of Pharmacology, Ribeirão Preto Medical School (FMRP), University of São Paulo (USP), Ribeirão Preto, São Paulo, Brazil;

4- Laboratory of Immunometabolism, Department of Genetics, Evolution, Microbiology and Immunology, Institute of Biology, University of Campinas (UNICAMP), São Paulo, Brazil;

5- Laboratory of Emerging Viruses, Department of Genetics, Evolution, Microbiology and Immunology, Institute of Biology, University of Campinas (UNICAMP), São Paulo, Brazil;

6- Department of Biochemistry and Immunology, Ribeirão Preto Medical School (FMRP), University of São Paulo (USP), Ribeirão Preto, São Paulo, Brazil;

7- Department of Biochemistry and Tissue Biology, Institute of Biology, University of Campinas (UNICAMP), Campinas, São Paulo, Brazil;

8- Laboratory of Immunoinflammation, Department of Genetics, Microbiology and Immunology, Institute of Biology, University of Campinas (UNICAMP), Campinas, São Paulo, Brazil;

9- Autoimmune Research Laboratory, Department of Genetics, Microbiology and Immunology, Institute of Biology, University of Campinas (UNICAMP), Campinas, São Paulo, Brazil;

10- Department of Pathology and Legal Medicine, Ribeirão Preto Medical School (FMRP), University of São Paulo (USP), Ribeirão Preto, São Paulo, Brazil;

11- Laboratory of Neuroimaging, Department of Neurology, University of Campinas (UNICAMP), Campinas, São Paulo, Brazil;

12- Department of Radiology, Clinical Hospital, University of Campinas (UNICAMP), Campinas, São Paulo, Brazil;

13- Institute of Mathematics, Statistics and Scientific Computation,.University of Campinas (UNICAMP), Campinas, São Paulo, Brazil;

14- Virology Research Center, Ribeirão Preto Medical School (FMRP), University of São Paulo (USP), Ribeirão Preto, São Paulo, Brazil;

15- Department of Cell and Molecular Biology, Ribeirão Preto Medical School (FMRP), University of São Paulo (USP), Ribeirão Preto, São Paulo, Brazil.

16- Department of Animal Biology, Institute of Biology, University of Campinas (UNICAMP), Campinas, São Paulo, Brazil;

17- Ribeirão Preto Clinics Hospital, Ribeirão Preto Medical School (FMRP), University of São Paulo, Ribeirão Preto, SP, Brazil;

18-Experimental Medicine Research Cluster (EMRC), University of Campinas (UNICAMP), Campinas, São Paulo, Brazil;

19- Obesity and Comorbidities Research Center (OCRC), University of Campinas (UNICAMP), Campinas, São Paulo, Brazil;

20- Department of Pharmacology, Institute of Biomedical Science, University of São Paulo (USP), São Paulo, Brazil;

21- D'Or Institute for Research and Education (IDOR), Rio de Janeiro, Brazil;

22- Institute of Biomedical Science (ICB), Federal University of Rio de Janeiro (UFRJ), Rio de Janeiro, Brazil;

23- Department of Clinical and Toxicological analyses, School of Pharmaceutical Sciences, University of Sao Paulo, São Paulo, SP, Brazil;

24- Department of Pathology, School of Medicine (FM), University of São Paulo (USP), São Paulo, Brazil;

25- National Institute for Biomarkers in Neuropsychiatry (INBioN), Brazilian National Council for Scientific and Technological Development (CNPq), Brazil;

26- D'Or Institute for Research and Education (IDOR), São Paulo, Brazil.

 # These authors contributed equally to this work.

***Correspondence should be addressed to:**

Daniel Martins-de-Souza, PhD: dmsouza@unicamp.br

Thiago Mattar Cunha, PhD: thicunha@fmrp.usp.br

Marcelo A. Mori, PhD: morima@unicamp.br

Clarissa Lin Yasuda, MD, PhD: cyasuda@unicamp.br

Abstract

One increasingly documented tendency of COVID-19 patients is to exhibit neuropsychiatric and neurological symptoms. Here we found that anxiety and cognitive impairment are manifested by 28-56% of COVID-19 convalescent individuals with mild respiratory symptoms and are associated with altered cerebral cortical thickness. Using an independent cohort, we found histopathological signs of brain damage in 25% of individuals who died of COVID-19. All of the affected brain tissue studied exhibited foci of SARS-CoV-2 infection and replication, particularly astrocytes. We also found that neural stem cell-derived human astrocytes *in vitro* are susceptible to SARS-CoV-2 infection through a mechanism that involves spike-NRP1 interaction. SARS-CoV-2-infected astrocytes manifested changes in energy metabolism and in key proteins and metabolites used to fuel neurons, as well as in the biogenesis of neurotransmitters. Moreover, infection elicits a secretory phenotype that reduces neuronal viability. Our data support the model in which SARS-CoV-2 reaches the brain, infects astrocytes and consequently leads to neuronal death or dysfunction. These deregulated processes are also likely to contribute to the structural and functional alterations seen in the brains of COVID-19 patients.

INTRODUCTION

COVID-19 is a disease caused by infection with the severe acute respiratory syndrome coronavirus 2 (SARS-CoV-2). Although the hallmark symptoms of COVID-19 are respiratory in nature and related to pulmonary infection, a growing body of evidence has demonstrated that SARS-CoV-2 has extrapulmonary effects (Gupta et al., 2020; Yang et al., 2020b) including in the central nervous system (CNS)(Nalbandian et al., 2021). Notably, over 30% of hospitalized

COVID-19 patients manifest neurological and even neuropsychiatric symptoms (Kotfis et al., 2020; Mao et al., 2020), and may eventually present some degree of encephalitis (Varatharaj et al., 2020). One study revealed that more than half of hospitalized patients continue to exhibit neurological symptoms as long as approximately three months after the acute stage (Lu et al., 2020). Impaired cognition was also confirmed in recovered patients after hospitalization (Batty et al., 2020; Mcloughlin et al., 2020; Pinna et al., 2020; Zhou et al., 2020) and neurological impairment is consistent with substantial damage to the nervous system (De Felice et al., 2020). Previous studies on Severe Acute Respiratory Syndrome (SARS) patients reported the presence of the SARS coronavirus in the brain tissue and cerebrospinal fluid of subjects who presented neurological symptoms (Hung et al., 2003; Lau et al., 2004; Xu et al., 2005). SARS-CoV-2 RNA was also detected in the cerebrospinal fluid of patients with meningitis (Bernard-Valnet et al.; Huang et al., 2020; Moriguchi et al., 2020). Moreover, alterations in the cerebral cortical region, compatible with viral infection (Politi et al., 2020), loss of white matter and axonal injury (Reichard et al., 2020), have all been reported in COVID-19 patients.

In line with the potential neurotropic properties of SARS-CoV-2, recent evidence demonstrated the presence of viral proteins in brain regions of COVID-19 patients and in the brains of K18-ACE2 transgenic mice infected with SARS-CoV-2 (Matschke et al., 2020; Song et al., 2020). The presence of SARS-CoV-2 in the human brain has been associated with significant astrogliosis, microgliosis and immune cell accumulation (Matschke et al., 2020). Further indicating the ability of SARS-CoV-2 to infect cells of the CNS, Song and colleagues showed that SARS-CoV-2 infects human brain organoid cells in culture (Song et al., 2020) Despite the accumulating evidence, little is known about the cellular and molecular mechanisms involved in SARS-CoV-2 infection of the brain and the consequent repercussions on brain structure and

functionality. To gain further insight into the neuropathological and neurological consequences of COVID-19 and possible cellular and molecular mechanisms, we performed a broad translational investigation associating clinical and brain imaging features of COVID-19 patients with neuropathological and biochemical changes caused by SARS-CoV-2 infection in the CNS. We found that astrocytes are the main sites of viral infection and replication within the CNS. SARS-CoV-2-infected astrocytes exhibited marked metabolic changes resulting in a reduction of metabolites used to fuel neurons and build neurotransmitters. Infected astrocytes also secrete an unidentified factor, or combination of factors, that leads to neuronal death. These events might be responsible for the neuropathological alterations and neuropsychiatric symptoms observed in COVID-19 patients.

RESULTS

Neuropsychiatric symptoms in convalescent COVID-19 patients correlate with altered cerebral cortical thickness

To explore the occurrences of brain damage in COVID-19 patients and dissociate it from the indirect consequences of the severe stage of the disease, we performed cortical surface-based morphometry analysis using high-resolution 3T MRI on 81 subjects diagnosed with COVID-19 who had mild respiratory symptoms and did not require hospitalization or oxygen support. The analysis was performed within an average (SD) interval of 57 (26) days after SARS-CoV-2 detection by RT-qPCR and the subjects were compared to 145 healthy volunteers collected pre-covid period (Tables S1 and S2). The analysis revealed areas of reduced cortical thickness in the left lingual gyrus; calcarine sulcus, including the cuneus; and olfactory sulcus, including the rectus gyrus (Figure 1A). In contrast, increased thickness was detected in the central sulcus,

including the precentral and postcentral gyrus, and superior occipital gyrus (Figure 1A), which can be associated with vasogenic edemas (Biega et al., 2006). A subgroup of these individuals (n = 61) were subjected to neuropsychological evaluation for anxiety (Beck Anxiety Inventory, BAI), depression (Beck Depression Inventory, BDI), logical memory (Wechsler Memory Scale), cognitive functions (TRAIL Making Test) and fatigue (Chalder Fatigue Questionnaire, CFQ). These tests were performed between 21 and 120 days after diagnosis (median of 59 days). Symptoms of anxiety were identified in approximately 28% of the subjects, and 20% of individuals presented symptoms of depression (Figure S1A). Nearly 28% of participants performed abnormally on the logical memory test and regarding cognitive function, approximately 34% and 56% performed abnormally with TRAIL A and B, respectively (Table S3 and Figure S1B).

When cortical thickness was studied alongside the data from the neurophysiological evaluation, a negative correlation was observed between BAI scores and cortical thickness of orbitofrontal regions (adjusted for CFQ) (Figure 1B and Table S4) and a positive correlation was observed between TRAIL B and cortical thickness of the right gyrus rectus (Figure 1C and Table S5). We additionally identified significant partial correlations between logical memory (immediate recall test, adjusted for BAI, BDI and CFQ) and cortical thickness of regions associated with language (Table S6). These results suggest that a thinner cortex in these areas is associated with poor performance on this verbal memory task. Overall, our findings indicate major alterations in cortical structure are associated with neuropsychiatric symptoms in COVID-19 patients with mild or no respiratory symptoms.

SARS-CoV-2 infects and replicates in human brain astrocytes of COVID-19 patients

Brain alterations in COVID-19 patients are hypothesized to be a consequence of either inflammatory or hemodynamic changes secondary to peripheral infection or SARS-CoV-2 invading the CNS and compromising cell viability and brain function. Although exacerbated inflammation and cardiovascular dysfunction have been well-characterized in COVID-19 patients who progress to the severe stages of the disease (Li et al., 2020), the degree of infection of the CNS by SARS-CoV-2 remains elusive. We performed a minimally invasive autopsy via endonasal trans-ethmoidal access to obtain brain samples from 26 individuals who died of COVID-19. Notably, these samples were from brain regions close to the areas in which we identified altered cortical thickness in the patients of the previous cohort. Initially, we performed an unbiased histopathological analysis of hematoxylin and eosin-stained brain sections to search for features of brain alterations. In our analyses, we observed alterations consistent with necrosis and inflammation in 25% of the brain tissues from these individuals (5 out of 26; Table S7). A deeper analysis revealed a strong predominance of senile changes such as corpora amylacea, lipofuscin deposits and parenchymal retraction around the vessels and the meninges. As brain sampling was performed via transsphenoidal by intranasal puncture, alternating white and gray matter was observed. The intraparenchymal inflammatory process was minimal, but present, represented by lymphocytes and perivascular microglia proliferation. In two cases, more intense inflammation was observed, delimiting tiny inflammatory aggregates, associated with endothelial hyperplasia or gemistocytic astrocytes. Cases with nasal epithelium sampled together with brain puncture demonstrated adaptive epithelial changes with cell balonization of the most superficial cells. Few cases showed small, multifocal areas of liquefaction necrosis (Figures 2A and S2A).

Next, we sought to evaluate the presence of SARS-CoV-2 in the five brain samples that presented histopathological alterations. Notably, SARS-CoV-2 genetic material and spike protein were detected in all five samples (Figures 2B and 2C). On average, SARS-CoV-2 spike protein was detected in 37% of the cells in the brain tissue (Figure 2D), the majority of these SARS-CoV-2 spike-positive cells (65.93%) being astrocytes (GFAP+ cells; Figures 2E and S2B). As such, approximately 25% of all cells in the brain samples of the five COVID-19 patients we analyzed were infected astrocytes. We also detected SARS-CoV-2 spike protein in neurons (NeuN+ cells; Figures 2E and S3A), but not in microglia (Iba-1+ cells; Figures 2E and S3B). The specificity of anti-spike antibodies was validated in brain tissue of COVID-19-free cases and in SARS-CoV-2-infected Vero cells (Figures S4A-S4C). Additionally, the presence of SARS-CoV-2 spike protein was directly correlated with the presence of double-stranded RNA (dsRNA) in the cells (Figures 2C and 2F), indicating the presence of replicative viruses in the brain tissue (Weber et al., 2006).

To confirm SARS-CoV-2 infects human astrocytes, we analyzed healthy human brain slices that were exposed to SARS-CoV-2. Both SARS-CoV-2 spike protein and double-stranded RNA were detected in human brain slices 48 hours post infection (Figure 3A). The SARS-CoV-2 genome was also detected by RT-PCR in brain slices infected at 24 and 48 hours post infection (Figure 3B). SARS-CoV-2 infection in astrocytes was confirmed by immunostaining the SARS-CoV-2 spike protein and GFAP (Figure 3C). We showed that the majority of the spike-positive cells (5.65% of total cells) were positive for GFAP (58.33% of infected cells; Figure 3D). Taken together, these data indicate that SARS-CoV-2 can preferentially infect astrocytes - and replicate within them - in human brain slices, which is in line with findings from human postmortem brains.

To obtain further evidence of the susceptibility of human astrocytes to SARS-CoV-2 infection, neural stem cell-derived human astrocytes (BR-1 cell line) were exposed to the virus and the viral load was determined at 24h after infection (Figure 4A). In agreement with what was observed in the *postmortem* brain samples, we confirmed that SARS-CoV-2 infects human astrocytes (Figures 4B-4E), shown by the detection of viral genetic material (Figure 4B) and spike protein in infected cells (Figures 4C and 4D). dsRNA was also observed in SARS-CoV-2-infected astrocytes *in vitro*, but not in mock-infected control cells, suggesting viral replication occurs in these cells (Figures 4C and 4E). We also observed that SARS-CoV-2 infection reduced human astrocyte viability by 25% after 48h post-infection, and remained at that reduced viability after 72h (Figure 4F). To confirm the susceptibility of human astrocytes to SARS-CoV-2 infection, we used a replication-competent pseudotyped vesicular stomatitis virus (VSV) in which the glycoprotein gene (G) of VSV was replaced by the full-length SARS-CoV-2 spike (S) and which contained a eGFP reporter (VSV-eGFP-SARS-CoV-2)(Case et al., 2020). Our data revealed that the human astrocyte culture was susceptible to VSV-eGFP-SARS-CoV-2 infection, supporting that human astrocytes are susceptible to SARS-CoV-2 infection (Figures 4G and 4H). We also evaluated viral replication in NSC-derived neurons and the SH-SY5Y cell line. The profile of astrocytes revealed a productive viral replication at 24h, maintained until 48h, showing effective viral replication (Figure 4C and S5A). The NSC-derived neurons, on the other hand, showed viral replication within 24h followed by a decrease in viral load (Figure S5B). Finally, the profile of SH-SY5Y indicated unproductive viral replication (Figure S5C). Altogether, these results indicate that human astrocytes are permissive cells for SARS-CoV-2 infection and may also represent a site for viral replication in the CNS.

NRP1 is required for infection of astrocytes by SARS-CoV-2

Since astrocytes are susceptible to SARS-CoV-2 infection, we searched for the cellular receptor involved in the viral entry mechanism. To do so, we started by using a publicly available single-cell RNAseq dataset from brain samples of COVID-19 patients (Yang et al., 2020a) to analyze the expression of classical SARS-CoV-2 receptors such as ACE2, as well as alternative receptors NRP1 and BSG (Cantuti-Castelvetri et al., 2020; Daly et al., 2020; Wang et al., 2020). These analyses revealed that ACE2 mRNA was undetected in astrocytes (data not shown)(Matschke et al., 2020; Yang et al., 2020a). However, astrocytes did express detectable levels of NRP1 and BSG mRNA (Figures 5A and 5B). We also found that the expression of NRP1 and BSG mRNA was increased in astrocytes from COVID-19 patients compared to controls (Figures 5A and 5B). Furthermore, the percentage of astrocytes expressing these receptors was also higher in the patients (Figures 5A and 5B). Since the binding of SARS-CoV-2 spike to BSG remains controversial (Shilts and Wright, 2020), we decided to explore the possible role of NRP1. Firstly, we performed Western blotting using cultured neural stem cell-derived astrocyte extracts to evaluate whether the single-cell RNAseq data was also seen in our *in vitro* model and confirmed at the protein level. We confirmed that human astrocytes do not express ACE2, whereas they do express NRP1 (Figures 5C-5E and S6). We used A549 cells transduced with ACE2 as the positive control. NRP1 receptor expression was seen to be markedly higher than the near-zero ACE2 expression in all cells (i.e., astrocytes, neural stem cell (NSC)-derived neurons and SH-SY5Y cells), and SARS-CoV-2 infection did not affect NRP1 or ACE2 expression (Figure 5D). To determine the role of NRP1 in the mechanisms behind SARS-CoV-2 infection in astrocytes, we pre-incubated these cells with a neutralizing, anti-NRP1 antibody. Neutralizing NRP1 in this manner inhibited the infection of astrocytes by SARS-CoV-2 (Figure

5F). Further supporting the participation of NRP1 in the infection of human astrocytes by SARS-CoV-2, we found that antibody-based neutralization of NRP1 also inhibited VSV-eGFP-SARS-CoV-2 infection of cultured astrocytes (Figures 5G and 5H). These results support the hypothesis that SARS-CoV-2 infects human astrocytes by interacting with the NRP1 receptor.

Proteomic and metabolomic changes in SARS-CoV-2-infected human astrocytes

To identify downstream mechanisms that are triggered by SARS-CoV-2 infection and, as such, possibly involved in the changes observed in the brain tissues of COVID-19 patients, we analyzed the proteome of SARS-CoV-2-infected human astrocytes (Figure 6A). Liquid chromatography-mass spectrometry (LC/MS)-based shotgun proteomics revealed 170 differentially expressed proteins in SARS-CoV-2-infected astrocytes compared to mock-control cells, being 68 upregulated and 102 downregulated (Figure S7A). A subset of the differentially expressed proteins showed sufficient differences to compose a molecular signature that was able to clearly distinguish the infected astrocytes from mock-controls (Figure 6A). Moreover, pathway enrichment and interactome analyses revealed that these proteins are involved in a wide range of biological processes and predicted regulatory networks affected by SARS-CoV-2 infection (Figure 6B). Pathways involved in carbon/glucose metabolism were among the most enriched (Figure 6C). NSC-derived neurons and SH-SY5Y cell lines were infected with SARS-CoV-2 and shown a different proteome profile (Figure S8A and S8B). Pathways enrichment analysis revealed higher similarity between NSC-derived neurons and SH-SY5Y cell lines when compared to NSC-derived astrocytes (S8C).

We also evaluated whether SARS-CoV-2 can trigger the same response as other neurotropic viruses, such as the Zika virus (ZIKV). In this case, we infected NSC-derived

astrocytes with SARS-CoV-2 and ZIKV with a MOI of 1.0. While overall protein identification provided high overlap, the statistically different proteins for each condition showed low similarity, indicating that the molecular changes induced by ZIKV and SARS-CoV-2 are distinct (Figures S9A-S9D). When the KEGG Pathway Database was used for analyses, the enriched pathways in SARS-CoV-2 and ZIKV showed little overlap; however when the Reactome Pathway Database was used, a higher overlap was observed between the enriched pathways. Altogether, these results demonstrate that SARS-CoV-2 and ZIKV elicit specific cell responses (Figure S9E).

We also conducted LC/MS proteomics with a separate set of samples consisting of 12 *postmortem* brain samples from COVID-19 patients *vs.* 8 SARS-CoV-2-negative controls. We identified 656 differentially expressed proteins, 117 downregulated and 539 upregulated. Pathways associated with neurodegenerative diseases, carbon metabolism and oxidative phosphorylation were enriched in these samples (Figure S7B). Notably, astrocytic proteins were the most present among the differentially expressed proteins, consistent with the higher frequency of infected astrocytes observed in COVID-19 *postmortem* brains (Figure 6D). Proteins found differentially expressed in SARS-CoV-2-infected astrocytes and in *postmortem* brain tissue samples were commonly associated with glycolysis/gluconeogenesis, carbon metabolism and the pentose phosphate pathway (Figure 6E). Collectively, these data indicate that SARS-CoV-2 infects astrocytes in the CNS, affecting energy metabolism and modulating proteins associated with neurodegeneration.

Since there are significant proteomic alterations in metabolic pathways, we sought to investigate whether the infection of human astrocytes would impact the levels of key metabolites involved in energy metabolism. LC/MS-based metabolomic analysis of SARS-CoV-2-infected

astrocytes showed marked changes in metabolic intermediates of glycolysis and anaplerotic reactions, indicating a remodeling of astrocyte metabolism (Figure 7A). This phenomenon was marked by the decrease in pyruvate and lactate, which are downstream metabolites of the glycolytic pathway, as well as a reduction in glutamine and intermediates of glutamine metabolism such as glutamate, GABA and alpha-ketoglutarate (Figure 7A). Despite these variations, there were no significant changes in tricarboxylic acid cycle (TCA cycle) intermediates (Figure S10). SARS-CoV-2 infected-astrocyte bioenergetics were further characterized by Seahorse Extracellular Flux analysis, showing increased respiration in infected cells (Figure 7B). This was due to an increase in both mitochondrial (maximal respiration) and non-mitochondrial oxygen consumption in SARS-CoV-2-infected astrocytes; the former was linked to higher proton leakage indicating increased uncoupled respiration (Figures 7B and 7C). Together, these results demonstrate increased metabolic activity in SARS-CoV-2-infected astrocytes and a reduction of metabolites used by these cells to support neuronal metabolism and function.

Conditioned medium from SARS-CoV-2-infected astrocytes reduces neuronal viability

Astrocytes are essential in the control of brain homeostasis, not only because they are the main energy reservoirs of the brain (Rouach et al., 2008) but also due to their important role in protective responses to cell damage triggered by infection or sterile inflammation (Liddelow et al., 2017; Yun et al., 2018). There is evidence that astrocytes secrete yet undetermined neurotoxic factors (Guttenplan et al., 2020a; Liddelow et al., 2017; Yun et al., 2018) and are also involved in the uptake, synthesis and distribution of brain metabolites (Gandhi et al., 2009; Simpson et al., 2007). Thus, we investigated whether neuronal viability could be indirectly affected by exposure to media conditioned by SARS-CoV-2-infected astrocytes. To test this

hypothesis, we cultured either NSC-derived neurons or differentiated SH-SY5Y neurons for 24 h in a control or conditioned medium, in which SARS-CoV-2-infected astrocytes were grown (Figure 8A). The conditioned medium increased the rate of apoptosis by 45.5% and 22.7% in NSC-derived neurons and SH-SY5Y neurons, respectively (Figures 8B-8E, and Figures S11A and S11B). This is despite the fact that NSC-derived neurons and SH-SY5Y neurons did not present a reduction in cell viability after 24h when directly exposed to SARS-CoV-2 (Figures 8D and 8E) nor was there a reduction in viability after 48h or 72h (Figures S11C and S11D). Nonetheless, neuronal exposure to the medium conditioned by SARS-CoV-2-infected astrocytes reduced the neuronal viability after 24h (Figure S11E). It is noteworthy that SARS-CoV-2 genetic material was not detected in SH-SY5Y neurons and NSC-derived neurons incubated with SARS-CoV-2-infected astrocyte-conditioned medium (Figures 8F and S11F), ruling out the possibility that neuronal death was due to infectious particles present in the conditioned medium. These results suggest that SARS-CoV-2-infected astrocytes release soluble factors which reduce neuronal viability.

DISCUSSION

Our study evidences structural and functional alterations in the brain tissue of COVID-19 patients which correlate with neuropsychiatric and neurological dysfunctions. This study and other reports showing alterations in brain structure and the manifestation of neurological symptoms in COVID-19 patients (Rogers et al., 2020; Troyer et al., 2020) raise a debate on whether these clinical features are a consequence of peripheral changes or the potential ability of the virus to invade the CNS. Our findings support the latter, at least in part, as we detect SARS-CoV-2 in brain tissue collected from patients who died of COVID-19. The ability of SARS-CoV-2 to infect brain cells has been demonstrated using *in vitro* models such as stem cell-

derived neural cells and cerebral organoids (Song et al., 2020). Viral particles have also been found in the brain (Matschke et al., 2020), localized to the microvasculature and neurons (Song et al., 2020), as well as in the choroid plexus (Jacob et al.) and meninges (Yavarpour-Bali and Ghasemi-Kasman, 2020). However, the magnitude of this infection and its distribution within brain tissue had not been demonstrated. Here we show that astrocytes are the main locus of infection - and possibly replication - of SARS-CoV-2 in COVID-19 patients' brains, as evidenced by the detection of the viral genome, the SARS-CoV-2 spike protein and dsRNA in both *postmortem* brain tissues and *in vitro* astrocytes. These findings are in line with recently published evidence showing that astrocytes from primary human cortical tissue and stem cell-derived cortical organoids are susceptible to SARS-CoV-2 infection (Andrews et al., 2021). Evidence was, however, insufficient to conclude if SARS-CoV-2 completes its replication cycle in astrocytes, warranting further experiments.

Recently, Meinhardt et al. 2021 described that SARS-CoV-2 could access the CNS through the neural–mucosal interface in olfactory mucosa, entering the primary respiratory and cardiovascular control centers in the medulla oblongata. Other proposed routes of SARS-CoV-2 neuro-invasion are through the infection of brain endothelial cells or the inflammatory response produced by SARS-CoV-2 infection, both causing dysfunctions in blood-brain barrier integrity (Alquisiras-Burgos et al., 2021; Meinhardt et al., 2021; Reynolds and Mahajan, 2021). At this point, there is much left to be learned about the routes of SARS-CoV-2 neuro-invasion and how the virus can navigate across those different brain cell types, producing manifestation of neurological symptoms in COVID-19 patients.

While ACE2 is the most well-characterized cellular receptor for the entry of SARS-CoV-2 into cells through the interaction with the viral spike protein, other receptors have also been

identified as mediators of infection (Hoffmann et al., 2020). According to our data and others (Matschke et al., 2020), astrocytes do not express ACE2, whereas we found higher expression of NRP1. This receptor is abundantly expressed in the CNS (Cantuti-Castelvetri et al., 2020; Daly et al., 2020; Wang et al., 2021), particularly in astrocytes and neurons (Figures 5D and 5E), and blocking its availability using neutralizing antibodies reduced SARS-CoV-2 infection in these cells. These results indicate that SARS-CoV-2 infects *in vitro* astrocytes via the NRP1 receptor, though this is yet to be proven *in vivo*.

To understand the consequences of SARS-CoV-2 infection in NSC-derived astrocytes, we searched for changes in the proteome in a non-hypothesis-driven fashion. SARS-CoV-2 infection resulted in substantial proteomic changes in several biological processes, including those associated with energy metabolism, in line with previous reports in other cell types infected with SARS-CoV-2 (Bojkova et al., 2020; Grenga et al., 2020; Stukalov et al., 2020). Noteworthily, differentially expressed proteins in COVID-19 *postmortem* brains were enriched for astrocytic proteins, strengthening our own findings that these are the most affected cells by SARS-CoV-2 infection in the human brain. Differentially expressed proteins in COVID-19 *postmortem* brains were also enriched for oligodendrocyte, neuron and Schwann cell markers, although less significantly when compared to astrocytes. Our proteomic data also evidenced changes in components of carbon metabolism pathways in both *in vitro* infected astrocytes and *postmortem* brain tissue from COVID-19 patients. These pathways were particularly associated with glucose metabolism.

Since astrocyte metabolism is key to support neuronal function, changes in astrocyte metabolism could indirectly impact neurons. One way astrocytes support neurons metabolically is by exporting lactate (Turner and Adamson, 2011) and one of the most critical alterations seen

here caused by SARS-CoV-2 infection in astrocytes was a decrease in pyruvate and lactate levels. Moreover, intermediates of glutamine metabolism such as glutamate and GABA were decreased in SARS-CoV-2-infected astrocytes. This said, there were no significant changes in any core intermediates of the TCA cycle. Together with the increased oxygen consumption rate of SARS-CoV-2-infected astrocytes, these results suggest that glycolysis and glutaminolysis are being used to fuel carbons into the TCA cycle to sustain the increased oxidative metabolism of infected astrocytes. Astrocyte-derived lactate and glutamine are required for neuronal metabolism (Gandhi et al., 2009; Suzuki et al., 2011) and synthesis of neurotransmitters such as glutamate and GABA, respectively (Walls et al., 2011). Astrocytes play a vital role in neurotransmitter recycling, a crucial process for the maintenance of synaptic transmission and neuronal excitability. This is especially important at glutamatergic synapses since proper glutamate uptake by astroglia prevents the occurrence of excitotoxicity (Bélanger et al., 2011). Upon this uptake, glutamine synthetase converts glutamate to glutamine, which can then be transferred back to neurons, thus closing the glutamate-glutamine cycle (Mergenthaler et al., 2013). This is also true for GABAergic synapses, where the neurotransmitter GABA is taken up by astrocytes and metabolized first to glutamate and then to glutamine (Bak et al., 2006). Moreover, astrocytes are responsible for maintaining glutamate levels in the brain (Bélanger and Magistretti, 2009; Magistretti, 2009). Hence, given the importance of the coupling between astrocytes and neurons, alterations in astrocytic glucose and glutamine metabolism are expected to compromise neuronal function, affecting neuronal metabolism and synaptic function and plasticity (Bonansco et al., 2011).

In addition to the metabolic changes observed in SARS-CoV-2-infected astrocytes that may impact neuronal dysfunction, we also found that SARS-CoV-2 infection elicits a secretory

phenotype in astrocytes that results in increased neuronal death. Our data points to the release of one or more still unidentified neurotoxic factors by SARS-CoV-2-infected astrocytes. A similar phenomenon has been observed when astrocytes are activated by inflammatory factors (Guttenplan et al., 2020b; Liddelow et al., 2017). Neuronal death may explain, at least partially, the alterations in cortical thickness we found in COVID-19 patients. A recent study with 60 recovered patients and 39 healthy controls also identified gray matter abnormalities 97 days after the onset of the disease, with increased volume in some areas of the brain (Lu et al., 2020). While that study analyzed hospitalized patients, we evaluated individuals that did not have to be hospitalized (i.e., had mild respiratory symptoms), and nevertheless, we observed notable alterations in cortical thickness. Importantly, some of these alterations correlated with severity of symptoms of anxiety and impaired cognition, which is consistent with previous literature (Knutson et al., 2015; Milad and Rauch, 2007). Since one of the hypotheses for the neuroinvasive mechanism of SARS-CoV-2 is via the olfactory nerves (Mao and Jin, 2020), we speculate that the associations between BAI and TRAIL B scores and structural alterations in the orbitofrontal region may be a result of the action of the virus in this cortical area, closely related to the olfactory nerves.

It is also worth noting that these regions are anatomically close to the brain regions from which we obtained *postmortem* samples (through endonasal trans-ethmoidal access) and identified histopathological alterations associated with SARS-CoV-2 infection. Our findings are consistent with a model in which SARS-CoV-2 is able to reach the CNS of COVID-19 patients, infects astrocytes and secondarily impairs neuronal function and viability. These changes might contribute to the alterations of brain structure as observed here and elsewhere, thereby resulting in the neurological and neuropsychiatric symptoms manifested by some COVID-19 patients. Our

study comes as a cautionary note that interventions directed to treat COVID-19 should also envision ways to prevent SARS-CoV-2 invasion of the CNS and/or replication in astrocytes.

Materials and Methods

Brain imaging and neuropsychological evaluation

Participants

Eighty-one patients (60 women, median 37 years of age) previously infected with SARS-CoV-2 were enrolled prospectively for this study after signing an informed consent form approved by the local ethics committee. These individuals presented mild symptoms during the acute phase and did not require hospitalization or oxygen therapy. They had a median interval of 54 days (range 16-120 days) between their RT-PCR exam and the day of MRI scanning and interview. For cortical thickness analysis, we included one hundred and forty-five controls (103 women, median 38 years of age) (Whelan et al., 2018) from our neuroimaging databank, given the difficulties and risk of recruiting healthy volunteers during the pandemic. The outpatients and healthy controls were balanced for age ($p=0.45$) and sex ($p=0.65$). The neuropsychological evaluations and neuroimaging analyses were approved by the Research Ethics Committee of the University of Campinas (CAAE: 31556920.0.0000.5404) and all subjects signed a consent form to participate.

Neuropsychological evaluation

We performed neuropsychological evaluations of sixty-one of these patients. They were tested for symptoms of anxiety using the Beck Anxiety Inventory (BAI) and symptoms of depression using the Beck Depression Inventory (BDI) (Garcia et al., 2019). Symptoms of

anxiety were confirmed for those with a BAI higher than 10 points, and depression symptoms defined for those with a minimum of 14 points on the BDI. Anxiety symptoms were considered mild (BAI 11-19), moderate (20-30) or severe (31-63) and depression symptoms were considered mild (BDI 14-19), moderate (20-35) or severe (36-63). We evaluated verbal memory (immediate and delayed episodic memory) using the Logical Memory subtest from the Wechsler Memory Scale (WMS-R) (Bolognani et al., 2015), in which the examiner verbally presents two stories, each including 25 pertinent pieces of information. Subjects are required to recall details of each story immediately after its presentation and again after 20 minutes. To evaluate other cognitive functions, we applied the TRAIL Making Test (TMT) (Llinàs-Reglà et al., 2017), which is subdivided into two steps. *Step A* assesses processing speed and visual search in a task that requires connecting 25 randomly arranged numbers in ascending order. *Step B* evaluates alternating attention and cognitive flexibility in a task associated with shifting rules in an ascending sequence of 25 numbers. A training stage is applied to both steps. We calculated z-scores for the results of these tests based on Brazilian normative data (Bolognani et al., 2015; Campanholo et al., 2014). For each test, the function was categorized as preserved (z-score > -0.99, including average, high average, above average and exceptionally high scores); low average score (z-score between -1 and -1.5); below-average score (z-score between -1.51 and -2); and exceptionally low score (z-score < -2) (Beauchamp et al., 2015; Guilmette et al., 2020). The Chalder Fatigue Questionnaire (CFQ-11) (Jackson, 2015) was used to evaluate fatigue in these subjects in which they were instructed to answer 11 questions (measured on a Likert scale 0-3), which yields a global score out of 33.

Neuroimaging analysis

We obtained the structural, 3D, T1-weighted images from a 3T Achieva-Philips MRI scanner (voxel size: 1x1x1 mm, TE = 3.2 ms, TR = 7 ms, matrix = 240x240x180, flip angle = 8 and FOV = 240x240 mm^2) (Garcia et al., 2019; Whelan et al., 2018). We performed imaging analyses with the CAT12 toolbox (http://www.neuro.uni-jena.de/cat/, version r1711) within SPM12 (http://www.fil.ion.ucl.ac.uk/spm/, version 7487) using MATLAB 2017b to extract Cortical Thickness (CT) maps, according to the default parameters. The T1 images were first spatially registered and segmented into gray matter, white matter and cerebrospinal fluid before calculating cortical thickness using the projection method described by Dahnke et al. (Righart et al., 2017). For voxelwise analysis of extracted maps, we used CAT12/SPM12 tools for an independent t-test (comparing COVID-19 patients and healthy controls), including age and sex as covariates. The results displayed were corrected for multiple comparisons using false discovery rate (FDR) (Genovese et al., 2002) correction ($p<0.05$). For anatomical identification, we used the Destrieux Atlas (2009) (Destrieux et al., 2010). Cortical parcellation was performed with standard CAT12 tools to extract the cortical thickness of regions of interest for correlations with neuropsychological scores. We used SPSS 22 for statistical analysis of clinical and neuropsychological variables. The FDR procedure was applied to adjust p-values for multiple comparisons (when necessary) with R software (Team, 2017).

Postmortem brain samples from COVID-19

Twenty-six individuals who died from complications related to COVID-19 were autopsied with an ultrasound-guided, minimally invasive approach using endonasal trans-ethmoidal access, performed within 1 hour of the patient's death. Brain tissue samples were

collected and fixed using a 10% neutral buffered formalin solution. After fixation, the tissue was embedded in a paraffin block and sectioned into slices with a thickness of 3µm. The sections were stained by H&E and immunofluorescence was observed. For proteomic analysis, twelve COVID-19 patients were autopsied using the same approach and frozen at -80°C. Brain tissue samples were collected and macerated in a lysis buffer (100mM Tris-HCl, pH 8.0, 150mM NaCl, mM EDTA, 0.5% Triton X-100) prior to trypsin digestion. The autopsy studies were approved by the National Commission for Research Ethics (CAAE: 32475220.5.0000.5440 and CAAE: 38071420.0.1001.5404).

Generation of human astrocytes (hES-derived)

Differentiation of glial progenitor cells was performed from neural stem cells (NSC) derived from pluripotent human embryonic stem cells (hES, BR-1 cell line) (Fraga et al., 2011), according to the method published by Trindade, 2020 (Trindade et al., 2020). NSCs were cultured in plates coated with Geltrex Matrix (Thermo Fisher Scientific, MA, USA) using 1:1 Neurobasal™/Advanced DMEM/F12 medium and 2% neural induction supplement. Upon reaching 50% confluence, the medium was changed to DMEM/F12 (Dulbecco's Modified Eagle Medium/F12), 1% N2 supplement, 1% fetal bovine serum (FBS), and 1% penicillin-streptomycin and maintained at 37°C in humidified air with 5% CO_2 for 21 days. At this stage, cells were considered glial progenitor cells (GPCs). Subsequently, GPCs were plated at low density (30-40% confluence) on Geltrex-coated plates and treated with DMEM/F12 medium, 1% GlutaMAX Supplement, 10% FBS and 1% penicillin-streptomycin. The differentiation medium was replaced every 2-3 days. After 4 weeks of differentiation, the cells were considered mature astrocytes. The cells were plated on Geltrex-coated coverslips at a density of $4x10^4$ cells for immunostaining assays (24-well plates) and $2.5x10^5$ cells for viral load, proteomic and

metabolomic analysis (6-well plates). All products used for cell culture are from Thermo Fisher Scientific, MA, USA. The characterization of the BR-1 lineage as astrocyte cells has been previously described elsewhere (Fraga et al., 2011; Ledur et al., 2020; Trindade et al., 2020; Yan et al., 2013). We generated eight batches of human astrocytes from BR-1-derived NSCs. The NSCs were of different passages and were used as biological replicates in independent experiments. Our internal control showed that about 97% of the neural stem cell-derived astrocytes in culture expressed GFAP, 80.4% expressed vimentin and 12.9% expressed SOX-2 (markers of progenitor cells). The neural stem cell-derived astrocyte culture expressed more astrocyte markers than progenitor cell markers, showing an excellent effectiveness of human astrocyte generation (hES-derived; Figure S12).

Virus strain

The HIAE-02-SARS-CoV-2/SP02/human/2020/BRA (GenBank accession number MT126808.1) virus strain was used for all *in vitro* experiments. The virus was isolated from the first confirmed case of COVID-19 in Brazil and kindly donated by Prof. Dr. Edison Durigon (ICB-USP). VSV-eGFP-SARS-CoV-2 was engineered and donated by Prof. Dr. Sean P.J. Whelan (Department of Medicine, Washington University School of Medicine, St. Louis, MO, USA) for SARS-CoV-2 entry experiments (Case et al., 2020). Viral stock was propagated in Vero CCL-81 cells (ATCC), cultivated in DMEM supplemented with 10% heat-inactivated FBS and 1% penicillin and streptomycin (Gibco, Walthmam, MA, USA) and incubated at 37°C with 5% CO_2 atmosphere. Viral titer was determined by the plaque-forming assay using Vero cells. The Brazilian ZIKV strain (BeH823339, 589; GenBank accession number KU729217) was used for proteomic experiments.

In vitro infection

Astrocytes were infected with SARS-CoV-2 for 1h using an MOI of 0.1 (proteomics; metabolomics; gene expression, viral load and bioenergetics assays; and flow cytometry analysis) or 1.0 (proteomics and immunostaining) under gentle agitation at room temperature. After viral adsorption, cells were washed twice with phosphate-buffered saline (PBS) and incubated with DMEM/F12 supplemented with 10% FBS, 1% GlutaMAX and 1% penicillin and streptomycin for 24h at standard culture conditions (37ºC and 5% CO_2 atmosphere). SARS-CoV-2 entry experiments were performed using SARS-CoV-2 (MOI 1.0) and VSV-eGFP-SARS-CoV-2 pseudotyped particles (MOI 1.0) in presence of a NRP1-neutralizing antibody (BD Bioscience, Cat. 743129, Clone U21-1283). We used anti-IgG2b as an antibody control (Biolegend, Cat. 406703, Clone RMG2b-1). Astrocytes were also infected with ZIKV for 1h using an MOI of 1.0 for proteomic experiments under gentle agitation at room temperature. We performed a comparison between SARS-CoV-2-infected astrocytes against ZIKV-infected astrocytes, using non-infected cells as controls. We chose ZIKV for the virus infection comparison due to the already well-described capability of ZIKV to infect the CNS and provoke several changes at a molecular level (Garcez et al., 2016).

Immunostaining and confocal microscopy

Brain sections from autopsies and astrocyte cell cultures were fixed with 10% neutral buffered formalin solution or 4% paraformaldehyde (PFA), respectively. Subsequently, the samples were incubated with primary antibodies: mouse monoclonal anti-GFAP Alexa Fluor 488 (EMD Millipore, clone GA5, Cat. MAB3402X, 1:400), human chimeric monoclonal anti-SARS-CoV-2 spike S1 (GeneScript, clone HC2001, Cat. A02038, 1:500), rabbit polyclonal anti-SARS-

CoV-2 spike (Rhea Biotech, Cat. IM-0828, 1:200), rabbit monoclonal anti-SARS-CoV-2 Spike (Invitrogen, clone T01KHuRb, Cat. 703959, 1:500), mouse monoclonal anti-double stranded RNA J2 (dsRNA, SCICONS English & Scientific Consulting Kft., clone J2-1909, Cat. 10010200; 1:1,000), rabbit polyclonal anti-IBA1 (FUJIFILM Wako Pure Chemical Corporation, Cat. 019-19741, 1:1,000) and rabbit monoclonal anti-NeuN (Abcam, clone EPR12763, Cat. Ab128886, 1:1,000). The slides were washed twice with TBS-T (Tris-Buffered Saline with Tween 20) and incubated with secondary antibodies donkey anti-mouse IgG AlexaFluor 647 (Thermo Fisher Scientific; Cat. A32787; 1:800) or AlexaFluor 488 (Abcam; Cat. ab150061; 1:800), donkey anti-rabbit IgG AlexaFluor 488 (Abcam; Cat. ab150065; 1:800) or AlexaFluor 594 (Abcam; Cat. ab150076; 1:800) and goat anti-human IgG FITC (Rhea Biotech, Cat. IC-3H04, 1:400). Controls were performed for secondary antibody fluorescence. Antibodies for detecting SARS-CoV-2 in human brain tissue and human astrocytes *in vitro* were first validated with SARS-CoV-2-infected and non-infected Vero cells. In addition, we validated the antibodies in brain sections from controls.

Nuclei were stained with DAPI (Life Technologies; Cat. D1306; 1:1,000). Images were acquired by an Axio Observer combined with an LSM 780 confocal device (Carl Zeiss) with 630x magnification and Z-stack (0.15µm) for brain sections. Colocalization analyses between GFAP and SARS-CoV-2 S1 or GFAP and dsRNA were quantified using the Fiji/ImageJ software. To determine colocalization, we used a ratio of GFAP:SARS-CoV-2 and GFAP:dsRNA in each sample by analyzing Pearson's correlation coefficients.

Western blots

Astrocytic cell culture samples were collected in RIPA Buffer (Sigma Aldrich, Cat. R0278) with protease and phosphatase inhibitors (Cell Signaling, Cat. 5872S). Protein content was quantified using a BCA protein assay kit (Sigma Aldrich, Cat. BCA1). Extracts were separated by 10% SDS-PAGE and transferred to nitrocellulose membranes. After transfering, the membranes were incubated at 4ºC with blocking buffer for 2h. The membranes were incubated in 5% BSA solution (Sigma Aldrich, Cat. A7906) and 0.1% Tween 20 (Sigma Aldrich, Cat. P2287) containing rabbit anti-ACE2 polyclonal antibody (Abcam; Cat. ab15348; 1:2,000) or rabbit anti-NRP1 monoclonal antibody (Abcam; clone EPR3113 Cat. ab81321; 1:1,000) overnight at 4ºC. Next, the membranes were incubated with anti-rabbit polyclonal antibody (Invitrogen; Cat. 31460; 1:5,000) for 1h. Finally, membranes were incubated with anti-beta-actin (Cell Signaling; clone 8H10D10; Cat. 3700) for 2h at room temperature. Beta-actin expression was used as loading control and was incubated post-ACE2/NRP1 without a stripping process. The membranes were detected with an ECL system (Millipore, Cat. WBULS0500) and Chemidoc imaging system (Bio-Rad Laboratories).

Human brain slice cultures

Cultures were prepared as previously described (Fernandes et al., 2019; Mendes et al., 2018). Cortical brain tissue was obtained from two patients who had an epileptic focus removed. A fragment of cortex was collected in the surgery room immediately after resection and transported to the laboratory. Tissue was sliced at 200µm in a VT1000s automatic vibratome (Leica) and cultivated free-floating with Neurobasal A (Gibco) medium supplemented with 1% Glutamax (Gibco), 1% penicillin/streptomycin (Gibco), 2% B27 (Gibco) and 0.25µg/mL fungizone

(Sigma). This procedure was approved by the Ethics Committee of the Ribeirao Preto Medical School (HCRP protocol #17578/15). For virus infection, the medium was removed, and the slices were exposed to TCID50 of $3x10^6$ for SARS-CoV-2 or an equivalent volume of mock medium. Infection was performed for 2h at 37°C, 5% CO_2 in a biosafety level 3 laboratory. The inoculum was removed, the tissue was washed and the slices were maintained in fresh medium at 37°C and 5% CO_2 until processing for subsequent analysis.

Single-cell transcriptomic analysis

We analyzed single-cell transcriptomic data from the brains of patients with COVID-19 and non-viral controls. The data was generated by Yang et al. (Yang et al., 2020a) and made publicly available at https://twc-stanford.shinyapps.io/scRNA_Brain_COVID19**.** The dataset was downloaded and the RDS file was imported into R environment version v3.6.3. Astrocyte cells were filtered based on cell type annotations provided by the original authors. To calculate the percentage of cells expressing BSG and NRP1, cell frequency was calculated considering cells with gene count ≥ 1 in the RNA essay for each gene (BSG and NRP1). Cells that met this criterion of minimum expression were considered as expressing the respective gene. A differential expression analysis was conducted using the FindMarkers function in Seurat with the Wilcoxon test comparing COVID-19 astrocyte cells vs non-viral astrocyte cells. Specifically, genes were calculated considering a minimum percent expression of genes in cells of 5% and average log fold change above 0.1. Genes were considered differentially expressed if the adjusted p-value was below 0.05.

Proteomics sample preparation, LC-MS/MS analyses and data processing

Astrocytes infected with SARS-CoV-2 and a mock control were collected in biological triplicate. Cells were chemically lysed with lysis buffer (100mM Tris-HCl, 1mM EDTA, 150mM NaCl, 1% Triton-X and protease and phosphatase inhibitors) and mechanically lysed with an ultrasonication probe during 3 cycles of 20s each with 90% frequency on ice. The total protein extract was quantified by BCA, according to the manufacturer's instructions (Thermo Fisher Scientific, MA, USA). 30µg of total protein extract from each sample was transferred to a Microcon-10 centrifugal filter with a 10kDa cutoff for FASP protein digestion (Distler et al., 2016). Briefly, proteins were reduced (10mM DTT) at 56°C for 40min, alkylated by 20 minutes in dark at a room temperature (50mM IAA) and digested overnight by trypsin at 37°C in 50mM ammonium bicarbonate (AmBic), pH 8.0. One the following day the peptides were recovered from the filter in 50mM AmBic, and trypsin activity was quenched by adding formic acid (FA) to a final concentration of 1% (v/v), whereupon the peptides were desiccated in a SpeedVac and stored at -80°C until use.

Digested peptides were resuspended in 0.1% FA. LC-MS/MS analyses were performed in an ACQUITY UPLC M-Class System (Waters Corporation, Milford, MA) coupled online to a Synapt G2-Si mass spectrometer (Waters Corporation, Milford, MA). 1µg of peptides were loaded onto a trapping column (Symmetry C18 5µm, 180µm × 20mm, Waters Corporation, Milford, MA) and subsequently separated in the analytical column (HSS T3 C18 1.8µm, 75µm × 150mm; Waters Corporation, Milford, MA). For gradient elutions, 0.1% FA was used as eluent A and acetonitrile-FA (99.9% ACN:0.1% FA) as eluent B. A reversed phase gradient was carried out during a 120-minute method, with a linear gradient 3 - 60% acetonitrile over 90min at 300nL/min. In the Synapt G2-Si, the peptide spectra were acquired by ion mobility-enhanced

data-independent acquisition ($HDMS^E$). Mass spectrometry analysis was performed in "Resolution Mode", switching between low (4eV) and high (25–60eV) collision energies, using a scan time of 1.0s per function over 50–2000m/z. The wave velocity for ion mobility separation was 1,000m/s and the transfer wave velocity was 175m/s. A [Glu1]-Fibrinopeptide B standard (Waters Corporation, Milford, MA) was used as the reference lock-mass compound. Each sample was run in three technical replicates.

The raw data from each experiment were processed in Progenesis QI for Proteomics (Waters Corporation, Milford, MA). Tandem mass spectra were searched against the *Homo sapiens* proteome database (UNIPROT, reviewed, release 2020-04), using tolerance parameters of 20ppm for precursor ions and 10ppm for product ions. For peptide identification, carbamidomethylation of cysteines was set as a fixed modification and oxidation of methionines as a variable modification, 2 missed cleavages were permitted and a false discovery rate (FDR) was limited to 1%. Protein identification was performed using a minimum of 1 fragment ion matched per peptide, a minimum of 3 fragment ions per protein and a minimum of 1 peptide per protein.

The label-free quantitative analysis was carried out using the relative abundance intensity normalized by all peptides identified. The expression analysis was performed considering the technical replicates for each experimental condition, following the hypothesis that each group is independent. Proteins with ANOVA $(p) \leq 0.05$ between groups were considered differentially expressed.

Bioinformatic analyses

Proteomic data visualization was performed in-house with the Python programming language (v. 3.7.3). Proteins differentially regulated ($p \leq 0.05$) were submitted to systems biology analysis in R (v. 4.0) and Cytoscape environments (Shannon et al., 2003). While performing the over-representation analysis (ORA), proteins were enriched using ClusterProfiler R package (Yu et al., 2012), CellMarker Database (Zhang et al., 2019) and Kyoto Encyclopedia of Genes and Genomes (KEGG) (Kanehisa and Goto, 2000). For the network analysis, it was run by Reactome Cytoscape plugin (Wu et al., 2010) for module detection and pathway enrichment analysis.

Metabolomics sample preparation, UPLC-MS/MS analyses and data processing

The astrocyte was washed twice with PBS at physiological pH, then the cells were collected with 600µL of methanol. Samples were dried and stored at -80°C until the metabolite extraction step. 473µL of water, 600µL of methanol and 1168µL of chloroform were added and the tubes were shaken vigorously for 2 minutes. Subsequently, samples were centrifuged for 5min at 13,000 x*g*. The aqueous supernatant and the organic phase (lower phase) were collected and dried for 60min and 40min, respectively, in a speed vacuum. All samples were stored at -80°C until analysis by LC-MS/MS.

The samples were resuspended in 100µL of a methanol:water mixture (1:1) and for each analysis, 4µL of the sample was injected. Sample separation was performed by hydrophobic interaction liquid chromatography (HILIC) using an Acquity UPLC® BEH amide column (1.7µm, 2.1mm x 100mm). The mobile phases used for the separations were ACN:H_2O (80:20) as mobile phase A and ACN:H_2O (30:70) as mobile phase B, both phases containing 10mM

ammonium formate and 0.1% ammonium hydroxide. Separation was then performed by a gradient from 99 - 1% buffer A over 7min. The column was returned to 99% buffer A for 2min for re-equilibration before the next injection for a total run time of 10min. Data acquisition was performed in negative mode and the instrument was operated in MS^E mode in the m/z range of 50–800Da, with an acquisition time of 0.1s per scan.

Identification of the metabolites of interest was carried out manually by spectral features, and the level 3 identification was obtained according to Schrimpe-Rutledge et al. (Schrimpe-Rutledge et al., 2016) using 5ppm as the error cutoff. The integration area of each peak was used to calculate the violin plot and an unpaired t-test with Welch's correction was used for statistical comparison. All analyses were performed using GraphPad Prism 8.0 software (San Diego, CA, USA) and a significance level of $p \leq 0.05$ was adopted.

RNA extraction, gene expression analyses and viral load

Total RNA extraction was performed using TRI Reagent according to the manufacturer's instructions (Sigma, St Louis, USA). RNA concentration was determined by a DeNovix spectrophotometer and RNA integrity was assessed by visualization of 28S and 18S ribosomal RNA on a 1% agarose gel. Reverse transcription was performed with 0.5µg of RNA using a GoScript reverse transcriptase kit (Promega, Madison, WI, USA) according to the manufacturer's instructions. qPCR was performed using astrocyte cDNA diluted 1:10 and the qPCR SybrGreen Supermix (Qiagen, Valencia, CA, USA) containing forward and reverse primers in RNAse-free water. All reactions were performed in a CFX384 Touch real-time PCR detection system (Biorad, Hercules, CA, USA) and cycling conditions were set as follows: 50°C for 2min; 95°C for 10min; (95°C for 15s; 60°C for 1min) x 40 cycles. To evaluate primer

specificity, a melting curve analysis was performed by heating samples from 65°C to 99°C (1°C increment changes at 5s intervals). All sample measurements were performed in duplicate. Primers were designed with PrimerBlast and used at a concentration of 200nM. Data were normalized to the expression of 18S (Fwd 5' CCCAACTTCTTAGAGGGACAAG 3'; Rev 5' CATCTAAGGGCATCACAGACC 3') and the relative quantification value of each target gene was determined using a comparative CT method (Schmittgen and Livak, 2008). For virus detection, SARS-CoV-2 nucleocapsid N1 primers were used as previously described (Fwd 5' CAATGCTGCAATCGTGCTAC 3'; Rev 5' GTTGCGACTACGTGATGAGG 3') (Codo et al., 2020; Won et al., 2020). The following primers sequences also were employed: *hACE2* (Fwd 5' GGACCCAGGAAATGTTCAGA 3'; Rev 5' GGCTGCAGAAAGTGACATGA 3') and *NRP1*(Fwd 5' GCCACAGTGGAACAGGTGAT 3'; Rev 5' ATGACCGTGGGCTTTTCTGT 3'). A serial dilution of SARS-CoV-2, *hACE2* and *NRP1 were* used as a standard curve.Data were expressed as mean ± SEM. Statistical significance was calculated by a two-tailed unpaired Student's t-test. All analyses were performed using GraphPad Prism 8.0 (San Diego, CA, USA) and a significance level of $p \leq 0.05$ was adopted.

Astrocyte bioenergetics

Astrocytes were plated on Seahorse XF-24 plates at a density of $1.5x10^4$ cells per well and incubated in complete culture medium for two days at 37°C in 5% CO_2. 24 hours before the experiment, cells were either infected by SARS-CoV-2 (MOI 0.1) or not infected (MOCK). One day post-infection, the culture medium was changed to Seahorse Base medium (supplemented with 1mM pyruvate, 2mM glutamine and 10mM glucose) and cells were incubated at 37°C in a non-CO_2 incubator for 1h. OCR (Oxygen Consumption Rate) was measured over the course of the experiment under basal conditions and after injections of oligomycin (1µM), FCCP (5µM)

and antimycin A/rotenone (100nM/1μM). Protein concentration was determined for each well to normalize the data. Data were expressed as mean ± SEM of two independent experiments performed in quintuplicate. Statistical significance was calculated by two-tailed unpaired Student's t-test. All analyses were performed using GraphPad Prism 8.0 software (San Diego, CA, USA) and a significance level of $p \leq 0.05$ was adopted.

Differentiation of the SH-SY5Y human neuroblastoma cell line

The SH-SY5Y cell line (SH-SY5Y-ATCC-CRL-2266) was cultivated using a commonly used neuronal differentiation protocol (Kovalevich and Langford, 2013; Shipley et al., 2016; Xicoy et al., 2017) using DMEM/F12 medium, 10% FBS and 1% penicillin-streptomycin at 37°C in humidified air with 5% CO_2. The SH-SY5Y cells were plated and, upon reaching 25-30% confluency, the medium was changed to neuronal differentiation medium consisting of DMEM/F12 with 1% FBS and 10μM retinoic acid (Sigma Aldrich). The differentiation medium was replaced every 2-3 days during 2 weeks. These differentiated SH-SY5Y cells are more closely related to adrenergic neurons, but they also express dopaminergic markers(Kovalevich and Langford, 2013). The SH-SY5Y cell line was kindly donated by Prof. Dr. Gustavo J. S. Pereira (Unifesp).

NSC differentiation into neurons

The human NSC-derived neurons were cultivated following the protocol described by Thermo Fisher Scientific (Brewer, 1995; Elkabetz and Studer, 2008; Trujillo et al., 2009). NSCs were plated on geltrex-coated plates and maintained with NEM medium at 37°C in humidified air with 5% CO_2. Upon reaching 40% confluency, the medium was changed to neuronal differentiation medium consisting of DMEM/F12 and Neurobasal medium (1:1) with 1% B27

supplement (Thermo Fisher Scientific, Carlsbad, CA, USA) and 1% Glutamax (Thermo Fisher Scientific, Carlsbad, CA, USA). The medium was renewed every four days for 20 days by removing half of the volume and adding the same volume of fresh medium. Medium renewal was performed in this manner since factors secreted by the differentiating cells are important for successful differentiation. Two control cell lines were used: GM23279A, obtained from a female subject (available at Coriell) and BR-1 (Fraga et al., 2011). Both cell lines were cultivated following the protocol described by Thermo Fisher Scientific (Casas et al., 2018; Goto-Silva et al., 2019; Ledur et al., 2020; White et al., 2020).

These cells and protocols have been extensively characterized elsewhere (Brewer, 1995; Elkabetz and Studer, 2008; Trujillo et al., 2009). We also used FACS analysis for cellular markers and found a bonafide neuronal phenotype due to the expression of the neuronal markers synaptophysin (75.9% of cells), MAP2 (99.9%) and β-tubulin (99%) and astrocytic marker GFAP (8.1%) (Figure S13).

CellTiter-Glo luminescent cell viability assay

Astrocyte and NSC-derived neuron death caused by SARS-CoV-2 infection was measured using ATP quantification by a luminescence assay (Promega, Madison, WI, USA; G7572). The CellTiter-Glo luminescent cell viability assay determines the number of viable cells in culture through quantitation of ATP levels, which reflect the presence of metabolically active cells. Astrocytes and NSC-derived neurons were infected with SARS-CoV-2 and harvested after 24, 48 or 72h. Astrocytes and NSC-derived neurons were then washed and the CellTiter-Glo reagent was added to the cells, following the manufacturer's instructions (Promega; G7572). The luminescent signals were obtained using a FlexStation 3 (Molecular Devices, CA, USA).

Calcein AM cell viability assay

SH-SY5Y death caused by SARS-CoV-2 infection was measured using Calcein AM, a cell-permeant dye that can be used to determine cell viability in most eukaryotic cells. In live cells, the non-fluorescent calcein AM is converted to green, fluorescent calcein, after acetoxymethyl ester hydrolysis by intracellular esterases (Invitrogen, Cat. No. C3100). The SH-SY5Y cell line was infected with SARS-CoV-2 and harvested after 24, 48 or 72h. SH-SY5Y cells were then washed and the approximately 2µM serum-free calcein AM working solution (FluoroBrite™ DMEM, ThermoFisher Scientific) was added to the cells and incubated for 30 minutes at room temperature, according to the manufacturer's protocol. The working solution was removed and replaced with normal growth medium. The fluorescence signals were obtained using a GloMax® Discover microplate reader (Promega, Madison, WI, USA).

Exposure of neurons to astrocyte-conditioned media

Astrocytes, human NSC-derived neurons and SH-SY5Y cells were cultured separately in standard conditions until complete differentiation. First, astrocytes were infected with SARS-CoV-2 (MOI 0.1 and MOI 1.0) or mock condition (MOCK), and after 24 hours, the medium was removed and cells were washed with PBS and cultured for 24 hours. The media of NSC-derived or SH-SY5Y neurons were removed and replaced by the conditioned media from SARS-CoV-2-infected astrocytes or control medium for 24 hours. After incubation, cells and their medium were collected for flow cytometry analysis, following the procedure described below.

Flow cytometry analyses

The expression of GFAP, synaptophysin, MAP2 and β-tubulin was evaluated through FACS analysis. Astrocytes and NSC-derived neurons were collected and stained with BD

Horizon fixable viability stain 510 for 30min at 4°C. Primary antibodies anti-GFAP (Abcam; Cat. Ab7260); anti-synaptophysin D35E4 (Cell Signaling; Cat.#5461); XP Rabbit mAb (Cell Signaling; Cat. #5461); anti-MAP2 (Abcam; Cat. ab32454); and anti-tubulin, beta III isoform, C-terminus (Milipore; Cat. #MAB1637) all diluted in BD Perm/Wash buffer, were added to the cells and incubated for 1h at 4°C (1:500). Secondary antibodies donkey anti-mouse IgG AlexaFluor 594 (Cell Signalling; Cat. 8890S), donkey anti-rabbit IgG AlexaFluor 647 (Abcam; Cat. ab15006) and donkey anti-goat IgG AlexaFluor 488 (Abcam; Cat. ab150129), all diluted in BD Perm/Wash buffer, were added and incubated for 30min at 4°C (1:250). Cells were washed with BD Perm/Wash buffer and then transferred to polypropylene FACS tubes. Analyses were carried out on a FACSymphony (Becton & Dickinson, San Diego, CA, USA)

The viability of human NSC-derived and SH-SY5Y neurons was determined 24h after incubation with the conditioned medium of SARS-CoV-2-infected astrocytes or control medium. The percentage of live (Apotracker-/FVS510-), necrotic (Apotracker-/FVS510+), early apoptotic (Apotracker+/FVS510-) and late apoptotic (Apotracker+/FVS510+) cells was determined by flow cytometry (FACSymphony, Becton & Dickinson, San Diego, CA, USA), after labeling with fixable viability stain (FVS510, BD Biosciences, #564406) and Apotracker Green (BioLegend, #427403). Data were analyzed using FlowJo software (BD Biosciences). Data are representative of at least two independent experiments performed in triplicate and are shown as mean ± SEM. P values were determined by one-way ANOVA followed by Tukey's post hoc test.

Data availability

The mass spectrometry proteomic data have been deposited to the ProteomeXchange Consortium via the PRIDE (Perez-Riverol et al., 2019) partner repository with the dataset identifiers PXD023781 and 10.6019/PXD023781.

ACKNOWLEDGMENTS

We thank Edison Durigon for providing the SARS-CoV-2 virus. We thank Gabriela Lopes Vitória, Elzira E. Saviani and Paulo Baldasso for technical support. The authors would like to thank FAPESP (São Paulo Research Foundation; grants 2020/04746-0; 2020/04860-8; 2017/25588-1; 2019/00098-7; 2014/10068-4; 2020/04919-2; 2013/08216-2; 2020/05601-6; 2020/04860-8; 2019/11457-8; 2013/07559-3; 2013/07607-8), FAEPEX (Fundo de Apoio ao Ensino, Pesquisa e Extensão, Unicamp; grant number 2274/20), CNPq (The Brazilian National Council for Scientific and Technological Development) and CAPES (Coordenação de Aperfeiçoamento de Pessoal de Nível Superior, Brazil). We dedicate this work to Dr. Nilton Barretos dos Santos, a brilliant scientist who was one of the many young victims of COVID-19.

AUTHOR CONTRIBUTIONS

F.C., V.C.C. and F.P.V. designed the majority of the experiments, performed the experiments, analyzed data and contributed to writing the manuscript. **P.H.V.** performed metabolomic analyses. **A.G.F.V., A.S.L.M.A., C.B-T., G.S.Z., G.R.-O., L.C.a, V.M.S-C., A.C.C.** contributed to the study design and performed experiments and data interpretation. **F.C., A.C.C., A.G.F.V., A.S.L.M.A., C.B-T., G.S.Z., V.M.S-C.** performed cell culture and cell differentiation, flow cytometry and RT-PCRs analyses. **A.S.L.M.A., A.C.C., P.L.P., D.A.T.T., G.F.S., S.P.M., R.G.L., J.F., M.R., N.B.S., M. C.M., R.E.M.P.S.** performed SARS-CoV-2 *in*

vitro infections and BSL-3 work. **R.G.L., G.P.R., T.L.K., G.G.D., J.A.G., P.B.R., N.B.S.** performed experiments and discussed the data. **V.C.C., G.R.O., L.C.** performed all proteomic experiments and *in silico* systems biology analyses. **R.B.J., L.S.S., M.H.N., I.K.A., M.R.B., M.K.M.A., J.R.S.J., L.L.D., M.E.P.C.S., I.M.P.S., E.D.R., S.M.G., L.H.L.S., V.B., B.M.C., F.C., C.L.Y.** recruited patients and performed brain imaging and clinical assessments. **G.L.** performed statistical analyses. **T.M., A.D-N., L.F.F.S., M.D., P.S.** collected human *postmortem* brain samples, assessed clinical files and discussed the data. **M.N.B., S.B., L.S., A.F.** collected human *postmortem* brain samples and performed histological analyses. **F.P.V., B.M.S.M., G.M.A., E.M.S.F., I.M.P., B.M.S.S., R.M.G., M.N.B., S.B., L.S., R.M.M.V., R.M., J.C.A-F., E.A., A.S., F.Q.C., T.M.C.** performed immunofluorescence, RT-PCR, histological and morphological analyses. **N.D.M., M.V.S., L.N.,** prepared and analysed the human brain slices. **I.M.S.C., H.I.N.** performed single-cell RNAseq bioinformatic analysis. **A.S.V., A.D., M.A.R.V., C.D.M., S.K.R., A.S.F., P.M.M.M-V., J.L.P.M.** conceived experiments, performed data interpretation, provided material and revised the paper. **M.A.M., T.M.C., D.M.S.** provided the funding for the study, formulated the hypothesis, designed experiments, analyzed data and wrote the manuscript with input from all authors. **D.M.S., T.M.C.** conceived and supervised the study.

DECLARATION OF INTERESTS

Authors declare no competing interests.

REFERENCES

Alquisiras-Burgos, I., Peralta-Arrieta, I., Alonso-Palomares, L.A., Zacapala-Gómez, A.E., Salmerón-Bárcenas, E.G., and Aguilera, P. (2021). Neurological Complications Associated with the Blood-Brain Barrier Damage Induced by the Inflammatory Response During SARS-CoV-2 Infection. Mol. Neurobiol. *58*, 520–535.

Andrews, M.G., Mukhtar, T., Eze, U.C., Simoneau, C.R., Perez, Y., Mostajo-Radji, M.A., Wang, S., Velmeshev, D., Salma, J., Kumar, G.R., et al. (2021). Tropism of SARS-CoV-2 for Developing Human Cortical Astrocytes. bioRxiv.

Bak, L.K., Schousboe, A., and Waagepetersen, H.S. (2006). The glutamate/GABA-glutamine cycle: aspects of transport, neurotransmitter homeostasis and ammonia transfer. Journal of Neurochemistry *98*, 641–653.

Batty, G.D., Deary, I.J., Luciano, M., Altschul, D.M., Kivimäki, M., and Gale, C.R. (2020). Psychosocial factors and hospitalisations for COVID-19: Prospective cohort study based on a community sample. Brain Behav. Immun. *89*, 569–578.

Beauchamp, M.H., Brooks, B.L., Barrowman, N., Aglipay, M., Keightley, M., Anderson, P., Yeates, K.O., Osmond, M.H., and Zemek, R. (2015). Empirical Derivation and Validation of a Clinical Case Definition for Neuropsychological Impairment in Children and Adolescents. J. Int. Neuropsychol. Soc. *21*, 596–609.

Bélanger, M., and Magistretti, P.J. (2009). The role of astroglia in neuroprotection. Dialogues Clin. Neurosci. *11*, 281–295.

Bélanger, M., Allaman, I., and Magistretti, P.J. (2011). Brain energy metabolism: focus on astrocyte-neuron metabolic cooperation. Cell Metab. *14*, 724–738.

Bernard-Valnet, R., Pizzarotti, B., Anichini, A., Demars, Y., Russo, E., Schmidhauser, M., Cerruti-Sola, J., Rossetti, A.O., and Du Pasquier, R. Two patients with acute meningo-encephalitis concomitant to SARS-CoV-2 infection.

Biega, T.J., Lonser, R.R., and Butman, J.A. (2006). Differential cortical thickness across the central sulcus: a method for identifying the central sulcus in the presence of mass effect and vasogenic edema. AJNR Am. J. Neuroradiol. *27*, 1450–1453.

Bojkova, D., Klann, K., Koch, B., Widera, M., Krause, D., Ciesek, S., Cinatl, J., and Münch, C. (2020). Proteomics of SARS-CoV-2-infected host cells reveals therapy targets. Nature *583*, 469–472.

Bolognani, S.A.P., Miranda, M.C., Martins, M., Rzezak, P., Bueno, O.F.A., Camargo, C.H.P. de, and Pompeia, S. (2015). Development of alternative versions of the Logical Memory subtest of the WMS-R for use in Brazil. Dement. Neuropsychol. *9*, 136–148.

Bonansco, C., Couve, A., Perea, G., Ferradas, C.Á., Roncagliolo, M., and Fuenzalida, M. (2011). Glutamate released spontaneously from astrocytes sets the threshold for synaptic plasticity.

European Journal of Neuroscience *33*, 1483–1492.

Brewer, G.J. (1995). Serum-free B27/neurobasal medium supports differentiated growth of neurons from the striatum, substantia nigra, septum, cerebral cortex, cerebellum, and dentate gyrus. Journal of Neuroscience Research *42*, 674–683.

Campanholo, K.R., Romão, M.A., Machado, M. de A.R., Serrao, V.T., Coutinho, D.G.C., Benute, G.R.G., Miotto, E.C., and de Lucia, M.C.S. (2014). Performance of an adult Brazilian sample on the Trail Making Test and Stroop Test. Dement Neuropsychol *8*, 26–31.

Cantuti-Castelvetri, L., Ojha, R., Pedro, L.D., Djannatian, M., Franz, J., Kuivanen, S., van der Meer, F., Kallio, K., Kaya, T., Anastasina, M., et al. (2020). Neuropilin-1 facilitates SARS-CoV-2 cell entry and infectivity. Science *370*, 856–860.

Casas, B.S., Vitória, G., do Costa, M.N., Madeiro da Costa, R., Trindade, P., Maciel, R., Navarrete, N., Rehen, S.K., and Palma, V. (2018). hiPSC-derived neural stem cells from patients with schizophrenia induce an impaired angiogenesis. Transl. Psychiatry *8*, 48.

Case, J.B., Rothlauf, P.W., Chen, R.E., Liu, Z., Zhao, H., Kim, A.S., Bloyet, L.-M., Zeng, Q., Tahan, S., Droit, L., et al. (2020). Neutralizing Antibody and Soluble ACE2 Inhibition of a Replication-Competent VSV-SARS-CoV-2 and a Clinical Isolate of SARS-CoV-2. Cell Host Microbe *28*, 475–485.e5.

Codo, A.C., Davanzo, G.G., Monteiro, L. de B., de Souza, G.F., Muraro, S.P., Virgilio-da-Silva, J.V., Prodonoff, J.S., Carregari, V.C., de Biagi Junior, C.A.O., Crunfli, F., et al. (2020). Elevated Glucose Levels Favor SARS-CoV-2 Infection and Monocyte Response through a HIF-1α/Glycolysis-Dependent Axis. Cell Metab.

Daly, J.L., Simonetti, B., Klein, K., Chen, K.-E., Williamson, M.K., Antón-Plágaro, C., Shoemark, D.K., Simón-Gracia, L., Bauer, M., Hollandi, R., et al. (2020). Neuropilin-1 is a host factor for SARS-CoV-2 infection. Science *370*, 861–865.

De Felice, F.G., Tovar-Moll, F., Moll, J., Munoz, D.P., and Ferreira, S.T. (2020). Severe Acute Respiratory Syndrome Coronavirus 2 (SARS-CoV-2) and the Central Nervous System. Trends Neurosci. *43*, 355–357.

Destrieux, C., Fischl, B., Dale, A., and Halgren, E. (2010). Automatic parcellation of human cortical gyri and sulci using standard anatomical nomenclature. Neuroimage *53*, 1–15.

Distler, U., Kuharev, J., Navarro, P., and Tenzer, S. (2016). Label-free quantification in ion mobility–enhanced data-independent acquisition proteomics. Nat. Protoc. *11*, 795–812.

Elkabetz, Y., and Studer, L. (2008). Human ESC-derived neural rosettes and neural stem cell progression. Cold Spring Harb. Symp. Quant. Biol. *73*, 377–387.

Fernandes, A., Mendes, N.D., Almeida, G.M., Nogueira, G.O., Machado, C. de M., Horta-Junior, J. de A. de C., Assirati Junior, J.A., Garcia-Cairasco, N., Neder, L., and Sebollela, A. (2019). Short-Term Free-Floating Slice Cultures from the Adult Human Brain. J. Vis. Exp.

Fraga, A.M., Sukoyan, M., Rajan, P., De Almeida Ferreira Braga, D.P., Iaconelli, A., Jr., Franco, J.G., Jr., Borges, E., Jr., and Pereira, L.V. (2011). Establishment of a Brazilian Line of Human Embryonic Stem Cells in Defined Medium: Implications for Cell Therapy in an Ethnically Diverse Population. Cell Transplant. *20*, 431–440.

Gandhi, G.K., Cruz, N.F., Ball, K.K., and Dienel, G.A. (2009). Astrocytes are poised for lactate trafficking and release from activated brain and for supply of glucose to neurons. J. Neurochem. *111*, 522–536.

Garcez, P.P., Loiola, E.C., Madeiro da Costa, R., Higa, L.M., Trindade, P., Delvecchio, R., Nascimento, J.M., Brindeiro, R., Tanuri, A., and Rehen, S.K. (2016). Zika virus impairs growth in human neurospheres and brain organoids. Science *352*, 816–818.

Garcia, D.D.S., Polydoro, M.S., Alvim, M.K.M., Ishikawa, A., Moreira, J.C.V., Nogueira, M.H., Zanão, T.A., de Campos, B.M., Betting, L.E.G.G., Cendes, F., et al. (2019). Anxiety and depression symptoms disrupt resting state connectivity in patients with genetic generalized epilepsies. Epilepsia *60*, 679–688.

Genovese, C.R., Lazar, N.A., and Nichols, T. (2002). Thresholding of statistical maps in functional neuroimaging using the false discovery rate. Neuroimage *15*, 870–878.

Goto-Silva, L., Ayad, N.M.E., Herzog, I.L., Silva, N.P., Lamien, B., Orlande, H.R.B., da Costa Souza, A., Ribeiro, S., Martins, M., Domont, G.B., et al. (2019). Computational fluid dynamic analysis of physical forces playing a role in brain organoid cultures in two different multiplex platforms. BMC Dev. Biol. *19*, 3.

Grenga, L., Gallais, F., Pible, O., Gaillard, J.-C., Gouveia, D., Batina, H., Bazaline, N., Ruat, S., Culotta, K., Miotello, G., et al. (2020). Shotgun proteomics analysis of SARS-CoV-2-infected cells and how it can optimize whole viral particle antigen production for vaccines. Emerg. Microbes Infect. *9*, 1712–1721.

Guilmette, T.J., Sweet, J.J., Hebben, N., Koltai, D., Mahone, E.M., Spiegler, B.J., Stucky, K., Westerveld, M., and Conference Participants (2020). American Academy of Clinical Neuropsychology consensus conference statement on uniform labeling of performance test scores. Clin. Neuropsychol. *34*, 437–453.

Gupta, A., Madhavan, M.V., Sehgal, K., Nair, N., Mahajan, S., Sehrawat, T.S., Bikdeli, B., Ahluwalia, N., Ausiello, J.C., Wan, E.Y., et al. (2020). Extrapulmonary manifestations of COVID-19. Nat. Med. *26*, 1017–1032.

Guttenplan, K.A., Weigel, M.K., Adler, D.I., Couthouis, J., Liddelow, S.A., Gitler, A.D., and Barres, B.A. (2020a). Knockout of reactive astrocyte activating factors slows disease progression in an ALS mouse model. Nat. Commun. *11*, 3753.

Guttenplan, K.A., Stafford, B.K., El-Danaf, R.N., Adler, D.I., Münch, A.E., Weigel, M.K., Huberman, A.D., and Liddelow, S.A. (2020b). Neurotoxic Reactive Astrocytes Drive Neuronal Death after Retinal Injury. Cell Rep. *31*, 107776.

Hoffmann, M., Kleine-Weber, H., Schroeder, S., Krüger, N., Herrler, T., Erichsen, S., Schiergens, T.S., Herrler, G., Wu, N.-H., Nitsche, A., et al. (2020). SARS-CoV-2 Cell Entry Depends on ACE2 and TMPRSS2 and Is Blocked by a Clinically Proven Protease Inhibitor. Cell.

Huang, Y.H., Hanna Huang, Y., Jiang, D., and Huang, J.T. (2020). SARS-CoV-2 Detected in Cerebrospinal Fluid by PCR in a Case of COVID-19 Encephalitis. Brain, Behavior, and Immunity *87*, 149.

Hung, E.C.W., Chim, S.S.C., Chan, P.K.S., Tong, Y.K., Ng, E.K.O., Chiu, R.W.K., Leung, C.-B., Sung, J.J.Y., Tam, J.S., and Dennis Lo, Y.M. (2003). Detection of SARS Coronavirus RNA in the Cerebrospinal Fluid of a Patient with Severe Acute Respiratory Syndrome. Clinical Chemistry *49*, 2108–2109.

Jackson, C. (2015). The Chalder Fatigue Scale (CFQ 11). Occup. Med. *65*, 86.

Jacob, F., Pather, S.R., Huang, W.-K., Wong, S.Z.H., Zhou, H., Zhang, F., Cubitt, B., Chen, C.Z., Xu, M., Pradhan, M., et al. Human Pluripotent Stem Cell-Derived Neural Cells and Brain Organoids Reveal SARS-CoV-2 Neurotropism.

Kanehisa, M., and Goto, S. (2000). KEGG: kyoto encyclopedia of genes and genomes. Nucleic Acids Res. *28*, 27–30.

Knutson, K.M., Dal Monte, O., Schintu, S., Wassermann, E.M., Raymont, V., Grafman, J., and Krueger, F. (2015). Areas of Brain Damage Underlying Increased Reports of Behavioral Disinhibition. J. Neuropsychiatry Clin. Neurosci. *27*, 193–198.

Kotfis, K., Williams Roberson, S., Wilson, J.E., Dabrowski, W., Pun, B.T., and Ely, E.W. (2020). COVID-19: ICU delirium management during SARS-CoV-2 pandemic. Crit. Care *24*, 176.

Kovalevich, J., and Langford, D. (2013). Considerations for the use of SH-SY5Y neuroblastoma cells in neurobiology. Methods Mol. Biol. *1078*, 9–21.

Lau, K.-K., Yu, W.-C., Chu, C.-M., Lau, S.-T., Sheng, B., and Yuen, K.-Y. (2004). Possible Central Nervous System Infection by SARS Coronavirus. Emerging Infectious Diseases *10*, 342–344.

Ledur, P.F., Karmirian, K., Pedrosa, C. da S.G., Souza, L.R.Q., Assis-de-Lemos, G., Martins, T.M., Ferreira, J. de C.C.G., de Azevedo Reis, G.F., Silva, E.S., Silva, D., et al. (2020). Zika virus infection leads to mitochondrial failure, oxidative stress and DNA damage in human iPSC-derived astrocytes. Sci. Rep. *10*, 1218.

Li, B., Yang, J., Zhao, F., Zhi, L., Wang, X., Liu, L., Bi, Z., and Zhao, Y. (2020). Prevalence and impact of cardiovascular metabolic diseases on COVID-19 in China. Clin. Res. Cardiol. *109*, 531–538.

Liddelow, S.A., Guttenplan, K.A., Clarke, L.E., Bennett, F.C., Bohlen, C.J., Schirmer, L.,

Bennett, M.L., Münch, A.E., Chung, W.-S., Peterson, T.C., et al. (2017). Neurotoxic reactive astrocytes are induced by activated microglia. Nature *541*, 481–487.

Llinàs-Reglà, J., Vilalta-Franch, J., López-Pousa, S., Calvó-Perxas, L., Torrents Rodas, D., and Garre-Olmo, J. (2017). The Trail Making Test. Assessment *24*, 183–196.

Lu, Y., Li, X., Geng, D., Mei, N., Wu, P.-Y., Huang, C.-C., Jia, T., Zhao, Y., Wang, D., Xiao, A., et al. (2020). Cerebral Micro-Structural Changes in COVID-19 Patients - An MRI-based 3-month Follow-up Study. EClinicalMedicine *25*, 100484.

Magistretti, P.J. (2009). Role of glutamate in neuron-glia metabolic coupling. The American Journal of Clinical Nutrition *90*, 875S – 880S.

Mao, X.-Y., and Jin, W.-L. (2020). The COVID-19 Pandemic: Consideration for Brain Infection. Neuroscience *437*, 130–131.

Mao, L., Jin, H., Wang, M., Hu, Y., Chen, S., He, Q., Chang, J., Hong, C., Zhou, Y., Wang, D., et al. (2020). Neurologic Manifestations of Hospitalized Patients With Coronavirus Disease 2019 in Wuhan, China. JAMA Neurol. *77*, 683–690.

Matschke, J., Lütgehetmann, M., Hagel, C., Sperhake, J.P., Schröder, A.S., Edler, C., Mushumba, H., Fitzek, A., Allweiss, L., Dandri, M., et al. (2020). Neuropathology of patients with COVID-19 in Germany: a post-mortem case series. Lancet Neurol.

Mcloughlin, B.C., Miles, A., Webb, T.E., Knopp, P., Eyres, C., Fabbri, A., Humphries, F., and Davis, D. (2020). Functional and cognitive outcomes after COVID-19 delirium. Eur. Geriatr. Med. *11*, 857–862.

Meinhardt, J., Radke, J., Dittmayer, C., Franz, J., Thomas, C., Mothes, R., Laue, M., Schneider, J., Brünink, S., Greuel, S., et al. (2021). Olfactory transmucosal SARS-CoV-2 invasion as a port of central nervous system entry in individuals with COVID-19. Nat. Neurosci. *24*, 168–175.

Mendes, N.D., Fernandes, A., Almeida, G.M., Santos, L.E., Selles, M.C., Lyra E Silva, N.M., Machado, C.M., Horta-Júnior, J.A.C., Louzada, P.R., De Felice, F.G., et al. (2018). Free-floating adult human brain-derived slice cultures as a model to study the neuronal impact of Alzheimer's disease-associated Aβ oligomers. J. Neurosci. Methods *307*, 203–209.

Mergenthaler, P., Lindauer, U., Dienel, G.A., and Meisel, A. (2013). Sugar for the brain: the role of glucose in physiological and pathological brain function. Trends Neurosci. *36*, 587–597.

Milad, M.R., and Rauch, S.L. (2007). The role of the orbitofrontal cortex in anxiety disorders. Ann. N. Y. Acad. Sci. *1121*, 546–561.

Moriguchi, T., Harii, N., Goto, J., Harada, D., Sugawara, H., Takamino, J., Ueno, M., Sakata, H., Kondo, K., Myose, N., et al. (2020). A first case of meningitis/encephalitis associated with SARS-Coronavirus-2. Int. J. Infect. Dis. *94*, 55–58.

Nalbandian, A., Sehgal, K., Gupta, A., Madhavan, M.V., McGroder, C., Stevens, J.S., Cook,

J.R., Nordvig, A.S., Shalev, D., Sehrawat, T.S., et al. (2021). Post-acute COVID-19 syndrome. Nat. Med. *27*, 601–615.

Perez-Riverol, Y., Csordas, A., Bai, J., Bernal-Llinares, M., Hewapathirana, S., Kundu, D.J., Inuganti, A., Griss, J., Mayer, G., Eisenacher, M., et al. (2019). The PRIDE database and related tools and resources in 2019: improving support for quantification data. Nucleic Acids Research *47*, D442–D450.

Pinna, P., Grewal, P., Hall, J.P., Tavarez, T., Dafer, R.M., Garg, R., Osteraas, N.D., Pellack, D.R., Asthana, A., Fegan, K., et al. (2020). Neurological manifestations and COVID-19: Experiences from a tertiary care center at the Frontline. J. Neurol. Sci. *415*, 116969.

Politi, L.S., Salsano, E., and Grimaldi, M. (2020). Magnetic Resonance Imaging Alteration of the Brain in a Patient With Coronavirus Disease 2019 (COVID-19) and Anosmia. JAMA Neurol. *77*, 1028–1029.

Reichard, R.R., Ross Reichard, R., Kashani, K.B., Boire, N.A., Constantopoulos, E., Guo, Y., and Lucchinetti, C.F. (2020). Neuropathology of COVID-19: a spectrum of vascular and acute disseminated encephalomyelitis (ADEM)-like pathology. Acta Neuropathologica *140*, 1–6.

Reynolds, J.L., and Mahajan, S.D. (2021). SARS-COV2 Alters Blood Brain Barrier Integrity Contributing to Neuro-Inflammation. J. Neuroimmune Pharmacol. *16*, 4–6.

Righart, R., Schmidt, P., Dahnke, R., Biberacher, V., Beer, A., Buck, D., Hemmer, B., Kirschke, J.S., Zimmer, C., Gaser, C., et al. (2017). Volume versus surface-based cortical thickness measurements: A comparative study with healthy controls and multiple sclerosis patients. PLoS One *12*, e0179590.

Rogers, J.P., Chesney, E., Oliver, D., Pollak, T.A., McGuire, P., Fusar-Poli, P., Zandi, M.S., Lewis, G., and David, A.S. (2020). Psychiatric and neuropsychiatric presentations associated with severe coronavirus infections: a systematic review and meta-analysis with comparison to the COVID-19 pandemic. Lancet Psychiatry *7*, 611–627.

Rouach, N., Koulakoff, A., Abudara, V., Willecke, K., and Giaume, C. (2008). Astroglial Metabolic Networks Sustain Hippocampal Synaptic Transmission. Science *322*, 1551–1555.

Schmittgen, T.D., and Livak, K.J. (2008). Analyzing real-time PCR data by the comparative C(T) method. Nat. Protoc. *3*, 1101–1108.

Schrimpe-Rutledge, A.C., Codreanu, S.G., Sherrod, S.D., and McLean, J.A. (2016). Untargeted Metabolomics Strategies-Challenges and Emerging Directions. J. Am. Soc. Mass Spectrom. *27*, 1897–1905.

Shannon, P., Markiel, A., Ozier, O., Baliga, N.S., Wang, J.T., Ramage, D., Amin, N., Schwikowski, B., and Ideker, T. (2003). Cytoscape: a software environment for integrated models of biomolecular interaction networks. Genome Res. *13*, 2498–2504.

Shilts, J., and Wright, G.J. (2020). No evidence for basigin/CD147 as a direct SARS-CoV-2

spike binding receptor.

Shipley, M.M., Mangold, C.A., and Szpara, M.L. (2016). Differentiation of the SH-SY5Y Human Neuroblastoma Cell Line. J. Vis. Exp. 53193.

Simpson, I.A., Carruthers, A., and Vannucci, S.J. (2007). Supply and demand in cerebral energy metabolism: The role of nutrient transporters. J. Cereb. Blood Flow Metab. *27*, 1766–1791.

Song, E., Zhang, C., Israelow, B., Lu-Culligan, A., Prado, A.V., Skriabine, S., Lu, P., Weizman, O.-E., Liu, F., Dai, Y., et al. (2020). Neuroinvasion of SARS-CoV-2 in human and mouse brain. bioRxiv.

Stukalov, A., Girault, V., Grass, V., Bergant, V., Karayel, O., Urban, C., Haas, D.A., Huang, Y., Oubraham, L., Wang, A., et al. (2020). Multi-level proteomics reveals host-perturbation strategies of SARS-CoV-2 and SARS-CoV.

Suzuki, A., Stern, S.A., Bozdagi, O., Huntley, G.W., Walker, R.H., Magistretti, P.J., and Alberini, C.M. (2011). Astrocyte-neuron lactate transport is required for long-term memory formation. Cell *144*, 810–823.

Team, R.C. (2017). RA language and environment for statistical computing. Versión 3.4. 3, Vienna, Austria, R Foundation for Statistical Computing.

Trindade, P., Loiola, E.C., Gasparotto, J., Ribeiro, C.T., Cardozo, P.L., Devalle, S., Salerno, J.A., Ornelas, I.M., Ledur, P.F., Ribeiro, F.M., et al. (2020). Short and long TNF-alpha exposure recapitulates canonical astrogliosis events in human-induced pluripotent stem cells-derived astrocytes. Glia *68*, 1396–1409.

Troyer, E.A., Kohn, J.N., and Hong, S. (2020). Are we facing a crashing wave of neuropsychiatric sequelae of COVID-19? Neuropsychiatric symptoms and potential immunologic mechanisms. Brain Behav. Immun. *87*, 34–39.

Trujillo, C.A., Schwindt, T.T., Martins, A.H., Alves, J.M., Mello, L.E., and Ulrich, H. (2009). Novel perspectives of neural stem cell differentiation: from neurotransmitters to therapeutics. Cytometry A *75*, 38–53.

Turner, D.A., and Adamson, D.C. (2011). Neuronal-astrocyte metabolic interactions: understanding the transition into abnormal astrocytoma metabolism. J. Neuropathol. Exp. Neurol. *70*, 167–176.

Varatharaj, A., Thomas, N., Ellul, M.A., Davies, N.W.S., Pollak, T.A., Tenorio, E.L., Sultan, M., Easton, A., Breen, G., Zandi, M., et al. (2020). Neurological and neuropsychiatric complications of COVID-19 in 153 patients: a UK-wide surveillance study. Lancet Psychiatry *7*, 875–882.

Walls, A.B., Eyjolfsson, E.M., Smeland, O.B., Nilsen, L.H., Schousboe, I., Schousboe, A., Sonnewald, U., and Waagepetersen, H.S. (2011). Knockout of GAD65 has major impact on synaptic GABA synthesized from astrocyte-derived glutamine. J. Cereb. Blood Flow Metab. *31*, 494–503.

Wang, C., Zhang, M., Garcia, G., Jr, Tian, E., Cui, Q., Chen, X., Sun, G., Wang, J., Arumugaswami, V., and Shi, Y. (2021). ApoE-isoform-dependent SARS-CoV-2 neurotropism and cellular response. Cell Stem Cell.

Wang, K., Chen, W., Zhou, Y.-S., Lian, J.-Q., Zhang, Z., Du, P., Gong, L., Zhang, Y., Cui, H.-Y., Geng, J.-J., et al. (2020). SARS-CoV-2 invades host cells via a novel route: CD147-spike protein.

Weber, F., Wagner, V., Rasmussen, S.B., Hartmann, R., and Paludan, S.R. (2006). Double-stranded RNA is produced by positive-strand RNA viruses and DNA viruses but not in detectable amounts by negative-strand RNA viruses. J. Virol. *80*, 5059–5064.

Whelan, C.D., Altmann, A., Botía, J.A., Jahanshad, N., Hibar, D.P., Absil, J., Alhusaini, S., Alvim, M.K.M., Auvinen, P., Bartolini, E., et al. (2018). Structural brain abnormalities in the common epilepsies assessed in a worldwide ENIGMA study. Brain *141*, 391–408.

White, J.A., 2nd, Krzystek, T.J., Hoffmar-Glennon, H., Thant, C., Zimmerman, K., Iacobucci, G., Vail, J., Thurston, L., Rahman, S., and Gunawardena, S. (2020). Excess Rab4 rescues synaptic and behavioral dysfunction caused by defective HTT-Rab4 axonal transport in Huntington's disease. Acta Neuropathol Commun *8*, 97.

Won, J., Lee, S., Park, M., Kim, T.Y., Park, M.G., Choi, B.Y., Kim, D., Chang, H., Kim, V.N., and Lee, C.J. (2020). Development of a Laboratory-safe and Low-cost Detection Protocol for SARS-CoV-2 of the Coronavirus Disease 2019 (COVID-19). Exp. Neurobiol. *29*, 107–119.

Wu, G., Feng, X., and Stein, L. (2010). A human functional protein interaction network and its application to cancer data analysis. Genome Biol. *11*, R53.

Xicoy, H., Wieringa, B., and Martens, G.J.M. (2017). The SH-SY5Y cell line in Parkinson's disease research: a systematic review. Molecular Neurodegeneration *12*.

Xu, J., Zhong, S., Liu, J., Li, L., Li, Y., Wu, X., Li, Z., Deng, P., Zhang, J., Zhong, N., et al. (2005). Detection of Severe Acute Respiratory Syndrome Coronavirus in the Brain: Potential Role of the Chemokine Mig in Pathogenesis. Clinical Infectious Diseases *41*, 1089–1096.

Yan, Y., Shin, S., Jha, B.S., Liu, Q., Sheng, J., Li, F., Zhan, M., Davis, J., Bharti, K., Zeng, X., et al. (2013). Efficient and rapid derivation of primitive neural stem cells and generation of brain subtype neurons from human pluripotent stem cells. Stem Cells Transl. Med. *2*, 862–870.

Yang, A.C., Kern, F., Losada, P.M., Maat, C.A., Schmartz, G., Fehlmann, T., Schaum, N., Lee, D.P., Calcuttawala, K., Vest, R.T., et al. (2020a). Broad transcriptional dysregulation of brain and choroid plexus cell types with COVID-19.

Yang, X., Yu, Y., Xu, J., Shu, H., Xia, J. 'an, Liu, H., Wu, Y., Zhang, L., Yu, Z., Fang, M., et al. (2020b). Clinical course and outcomes of critically ill patients with SARS-CoV-2 pneumonia in Wuhan, China: a single-centered, retrospective, observational study. Lancet Respir Med *8*, 475–481.

Yavarpour-Bali, H., and Ghasemi-Kasman, M. (2020). Update on neurological manifestations of COVID-19. Life Sci. *257*, 118063.

Yu, G., Wang, L.-G., Han, Y., and He, Q.-Y. (2012). clusterProfiler: an R package for comparing biological themes among gene clusters. OMICS *16*, 284–287.

Yun, S.P., Kam, T.-I., Panicker, N., Kim, S., Oh, Y., Park, J.-S., Kwon, S.-H., Park, Y.J., Karuppagounder, S.S., Park, H., et al. (2018). Block of A1 astrocyte conversion by microglia is neuroprotective in models of Parkinson's disease. Nat. Med. *24*, 931–938.

Zhang, X., Lan, Y., Xu, J., Quan, F., Zhao, E., Deng, C., Luo, T., Xu, L., Liao, G., Yan, M., et al. (2019). CellMarker: a manually curated resource of cell markers in human and mouse. Nucleic Acids Res. *47*, D721–D728.

Zhou, F., Yu, T., Du, R., Fan, G., Liu, Y., Liu, Z., Xiang, J., Wang, Y., Song, B., Gu, X., et al. (2020). Clinical course and risk factors for mortality of adult inpatients with COVID-19 in Wuhan, China: a retrospective cohort study. Lancet *395*, 1054–1062.

Table 1. Reduced cortical thickness in the left hemisphere

Value (T statistic)	Cluster size (number of voxels)	Overlap of atlas region	Anatomical correspondence
5	193	G_oc-temp_med-Lingual	Lingual gyrus
4.6	77	S_calcarine	Calcarine sulcus
		G_cuneus	Cuneus
		S_parieto_occipital	Parieto-occipital sulcus
4	26	S_orbital_med-olfact	Olfactory sulcus
		G_rectus	Rectus gyrus

Table 2. Increased cortical thickness in the right hemisphere

Value (T statistic)	Cluster size (number of voxels)	Overlap of atlas region	Anatomical correspondence
5.4	277	S_central	Central sulcus
		G_precentral	Precentral gyrus
		G_postcentral	Postcentral gyrus
4.2	40	G_occipital_sup	Superior occipital gyrus
		G_cuneus	Cuneus

Table 3. Results of Neuropsychological tests (in z-score)

	Median	Range
Logical memory (immediate recall)	-0.63	-2.25 to 1.96
Logical memory (delayed recall)	-0.27	-2.37 to 1.58
TRAIL A	-0.7	-7 to 0.77
TRAIL B	-1.13	-5.55 to 1.25

Table 4. Correlations between BAI scores and cortical thickness of orbitofrontal regions

	Correlation	Significance	FDR adjusted significance
Left orbital gyrus	-0.19	0.2	0.4
Right orbital gyrus	-0.42	0.004	0.016
Left gyrus rectus	-0.017	0.91	0.91
Right gyrus rectus	-0.1	0.5	0.67

FDR: false discovery rate

Table 5. Correlations between TRAIL B scores and thickness of gyrus rectus

	Correlation	Significance	FDR adjusted significance
Left gyrus rectus	0.1	0.43	0.43
Right gyrus rectus	0.32	0.014	0.03

FDR: false discovery rate

Table 6. Correlations between Logical memory (immediate recall) scores and cortical thickness of IFG and STG.

	Correlation	Significance	FDR adjusted significance
Left IFG (pars opercularis)	0.27	0.08	0.1
Right IFG (pars opercularis)	0.28	0.07	0.1
Left IFG (pars triangularis)	0.35	0.02	0.04
Right IFG (pars triangularis)	0.43	0.004	0.02
Left STG (planum temporale)	0.39	0.01	0.03
Right STG (planum temporale)	0.25	0.12	0.12

IFG: inferior frontal gyrus; STG: superior temporal gyrus; FDR; false discovery rate

Table 7 : COVID-19 patient characteristics

Demographics		**%**
Number	26	
Age (years)	66.08±14.89	
Hospital day	12.8±10.08	
Female	10	38.46%
Comorbities		
Hypertension	20	76.92%
Diabetes	13	50%
Obesity	12	46%
Lung disease	2	7.69%
History of smoking	8	30.76%
Heart disease	10	38.46%
Kidney disease	5	19.23%
Cerebrovascular accident	4	15.38%
Cancer	2	7.69%
Autoimmune diseases	3	11.53%
Immune deficiency	2	7.69%
Laboratory findings		
CRP (mg/dL)*	13.81±7.125	
D-Dimers (µg/mL)**	3.84±2.94	
LDH (U/L)#	631.6±481.2	
Ferritin (ng/mL)&	1,566±1,381	
Haemoglobin (g/dL)	11.73±2.33	
Neutrophils (cell/mm^3)	7,632±4,474	
Lymphocytes (cell/mm^3)	2,955±9,053	
Platelets (count/mm^3)	201,682±122,865	
Medications		
Antibiotics	25	96.1%
Heparin	25	96.1%
Antimalarial	1	3.84%
Oseltamivir	15	57.69%
Glucocorticoids	11	42.30%
Respiratory status		
Mechanical ventilation	26	100%
Nasal-cannula oxygen	22	84.61%
pO_2	74.45±18.13	
$SatO_2$	91.80±7.859	
Outcome		
Deaths	26	100%

**CRP: C-reactive protein (Normal value <0.5 mg/dL);*
***D-dimers (NV <0.5 µg/mL); #LDH: lactic dehydrogenase (Normal range: 120-246 U/L); &Ferritin (NR: 10-291 ng/mL)*

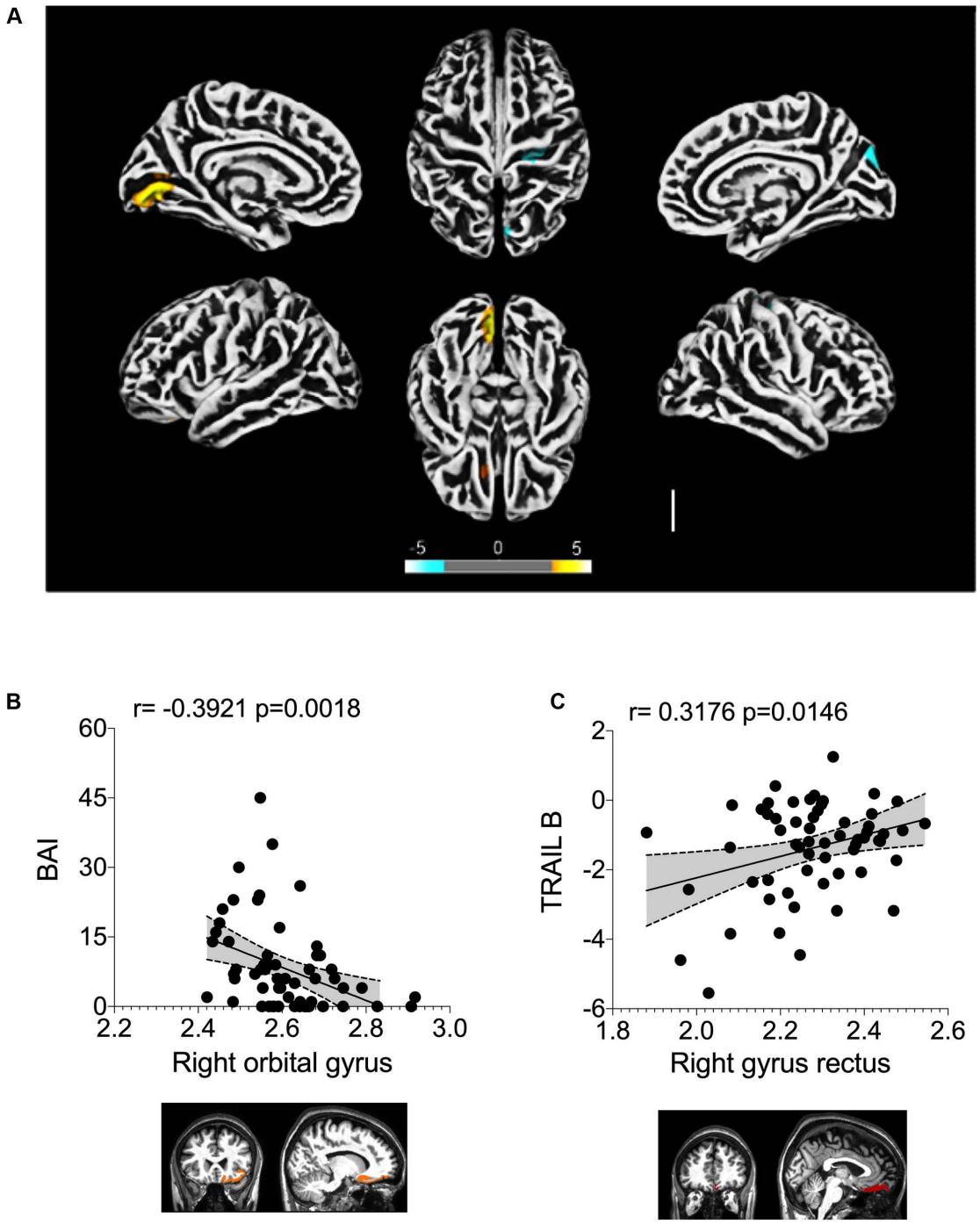

Figure 1. Altered cerebral cortical thickness is associated with neuropsychiatric symptoms in COVID-19 patients.

(A) Surface-based morphometry using high-resolution 3T MRI. Yellow represents areas of decreased cortical thickness: left lingual gyrus, calcarine sulcus (and cuneus) and olfactory sulcus (and rectus gyrus). Blue represents areas of increased cortical thickness: central sulcus (precentral and postcentral gyrus) and superior occipital gyrus. Representative image of the analysis of 81 subjects who tested positive for SARS-CoV-2 (who had mild respiratory symptoms and did not require hospitalization or oxygen support) compared to 145 healthy volunteers (without diagnosis of COVID-19). The analysis was performed within an average (SD) interval of 57.23 (25.91) days.

(B) Correlation between anxiety scores (BAI) and right orbital gyrus thickness. The data depicts Pearson's correlation coefficient and region of interest in representative images.

(C) Correlation between TRAIL B cognitive performance scores and right gyrus rectus thickness. Data depict Pearson's correlation coefficient and region of interest in representative images.

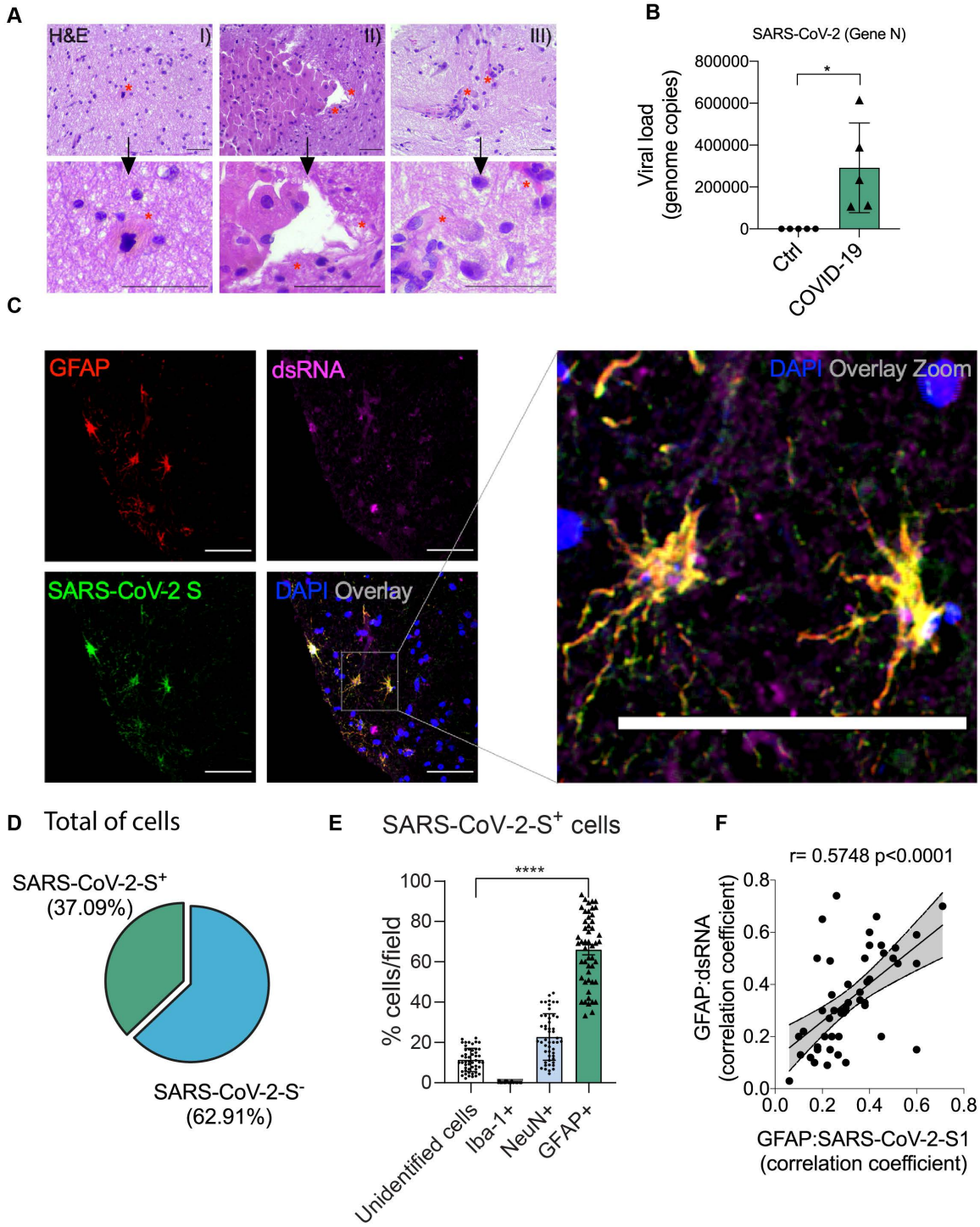

Figure 2. SARS-CoV-2 infects the central nervous system, replicates in astrocytes and causes brain damage.

(A) Histopathological H&E images of *postmortem* brain tissue from individuals who died of

COVID-19. Five out of 26 individuals showed signs of brain damage as represented in the images by (I) areas of necrosis, cytopathic damage (i.e., enlarged, hyperchromatic, atypical-appearing nuclei), vessels with margination of leukocytes and thrombi (II) and an infiltration of immune cells (III). The alterations are indicated by red asterisks and a respective zoom. Images were acquired with 400x magnification. Scale bar indicates 50 µm.

(B) Viral load in brain tissues from the five COVID-19 patients who manifested histopathological alterations in the brain as compared to samples from SARS-CoV-2-negative controls (n=5 per group).

(C) Representative confocal images of the brain tissue of one COVID-19 patient who manifested histopathological alterations. Immunofluorescence targeting glial fibrillary acidic protein (GFAP, red), double-stranded RNA (dsRNA, magenta), SARS-CoV-2-S (green), and nuclei (DAPI, blue). Images were acquired with 630x magnification. Scale bar indicates 50 µm.

(D) Percentage of SARS-CoV-2-S positive cells in this tissue.

(E) Percentage of GFAP-positive *vs.* unidentified cells, Iba1 and NeuN among infected cells. Ten fields/cases were analyzed.

(F) Pearson's correlation coefficient demonstrating colocalization of SARS-CoV-2-S and dsRNA within GFAP-positive cells.

All data are shown as mean ± SEM. P-values were determined by two-tailed unpaired tests with Welch's correction (B) or ANOVA one-way followed by Tukey's post hoc test (E).*$P < 0.05$ compared to the control group; **** $P < 0.0001$ compared to unidentified cells, Iba1 and NeuN groups.

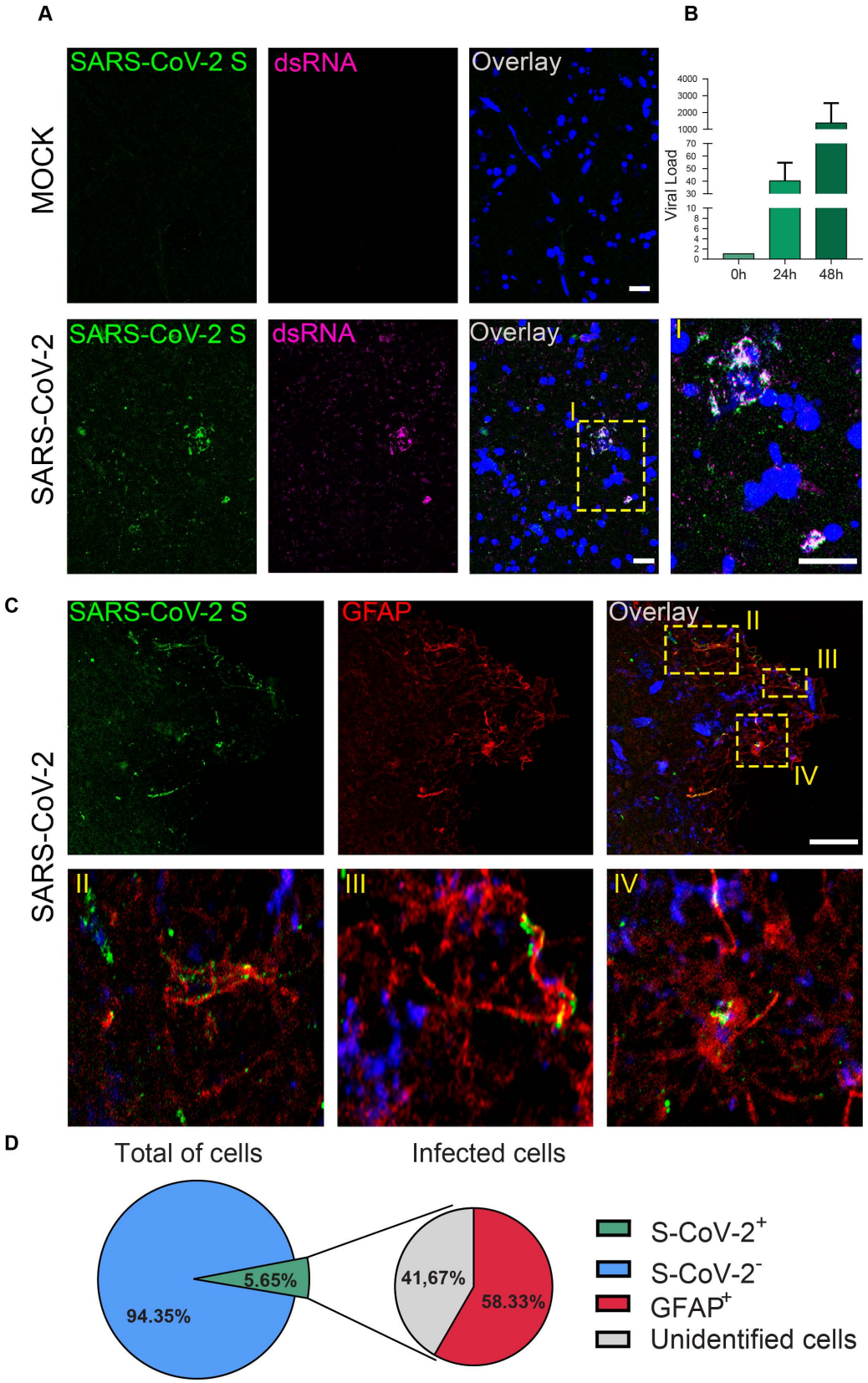
A
B
MOCK
SARS-CoV-2
SARS-CoV-2 S
dsRNA
Overlay
Viral Load
0h
24h
48h
I
C
GFAP
II
III
IV
D
Total of cells
Infected cells
5.65%
94.35%
41,67%
58.33%
S-CoV-2+
S-CoV-2-
GFAP+
Unidentified cells

Figure 3. SARS-CoV-2 infects, replicates and preferentially targets astrocytes in adult human brain slices.

(A) Representative images of uninfected control (mock) and SARS-CoV-2-infected human brain slices. Tissue sections were stained for SARS-CoV-2 spike protein (green), double stranded RNA (magenta), and nuclei (DAPI, blue), as indicated. Scale bar indicates 20 µm. Higher magnification is shown in I.

(B) Viral load determined by RT-PCR in a human brain slice infected by SARS-CoV-2 at 0, 24 and 48 hours post infection compared to mock-slices (n=2 slices from one patient).

(C) Representative cells double-labeled with SARS-CoV-2 spike protein (green) and GFAP (red) are shown at a higher magnification in II, III and IV.

(D) Quantification of cells positive for SARS-CoV-2 spike protein and GFAP in human brain slices (n= 2 fields from one patient). Scale bar indicates 20 µm.

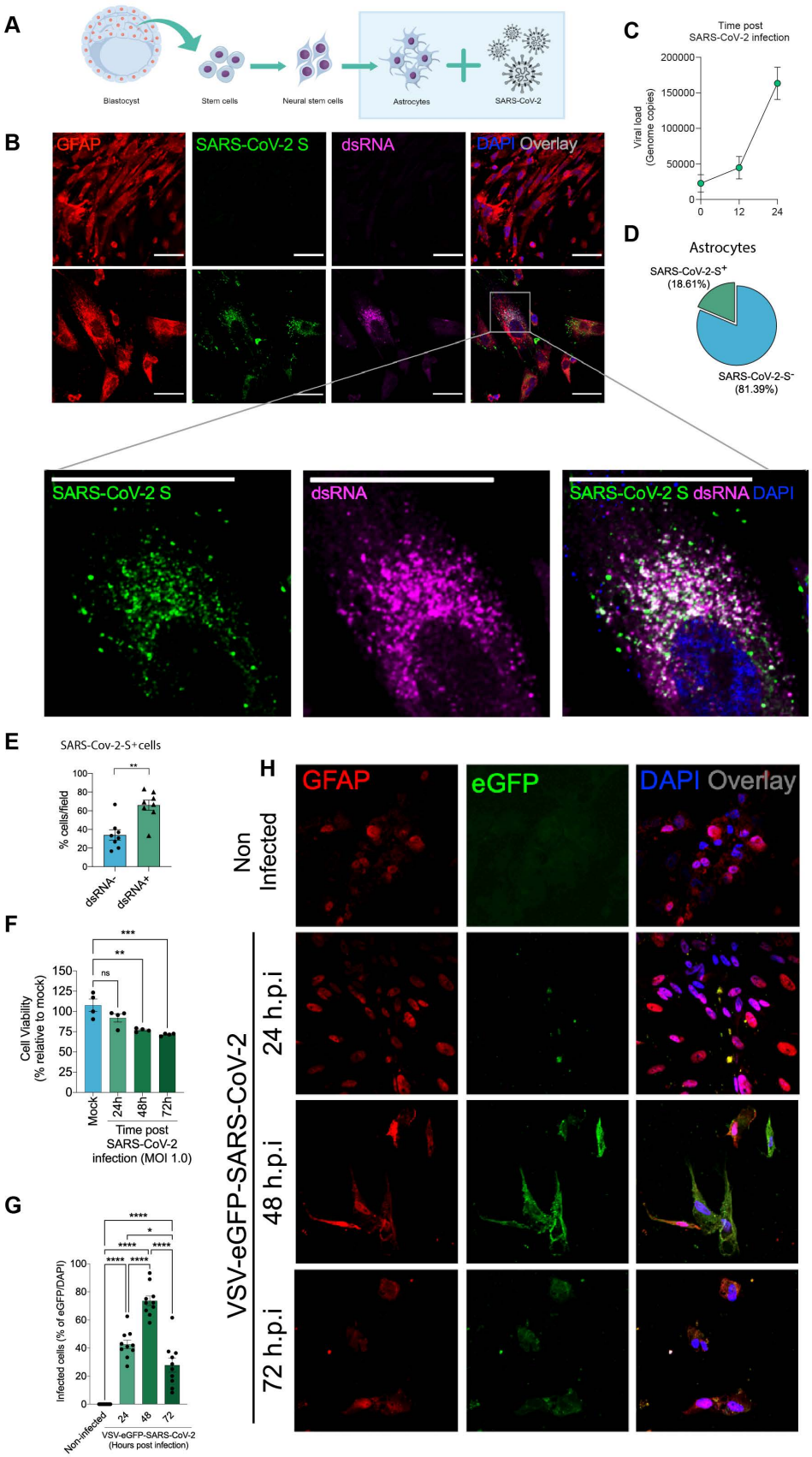
A
Blastocyst
Stem cells
Neural stem cells
Astrocytes
SARS-CoV-2
B
GFAP
SARS-CoV-2 S
dsRNA
DAPI Overlay
SARS-CoV-2 S
dsRNA
SARS-CoV-2 S dsRNA DAPI
C
Time post SARS-CoV-2 infection
Viral load (Genome copies)
200000
150000
100000
50000
0
0
12
24
D
Astrocytes
SARS-CoV-2-S+ (18.61%)
SARS-CoV-2-S- (81.39%)
E
SARS-Cov-2-S+cells
% cells/field
dsRNA-
dsRNA+
F
Cell Viability (% relative to mock)
Mock
24h
48h
72h
Time post SARS-CoV-2 infection (MOI 1.0)
ns
G
Infected cells (% of eGFP/DAPI)
Non-infected
24
48
72
VSV-eGFP-SARS-CoV-2 (Hours post infection)
H
GFAP
eGFP
DAPI Overlay
Non Infected
VSV-eGFP-SARS-CoV-2
24 h.p.i
48 h.p.i
72 h.p.i

Figure 4. SARS-CoV-2 infects and replicates in astrocytes *in vitro*.

(A) Human neural stem cell-derived astrocytes were infected *in vitro* with SARS-CoV-2 (MOI 1.0) for 1h, washed and harvested 24h after infection.

(B) Immunostaining for GFAP (red), double-stranded RNA (dsRNA, magenta), SARS-CoV-2-S (green) and nuclei (DAPI, blue). Images were acquired with 630x magnification. Scale bar indicates 50 µm.

(C) SARS-CoV-2 viral load detection in astrocyte cell pellets (n = 6 replicates) using RT-PCR.

(D) Percentage of infected astrocytes. The data depict SARS-CoV-2-S and DAPI-stained cells (100 fields were analyzed).

(E) Frequency of cells containing replicating viruses.

(F) Astrocyte viability upon SARS-CoV-2 infection was assessed using a luminescence-based cell viability assay (CellTiter-Glo), determining the number of live cells by quantification of ATP at 24, 48 and 72 hours post infection.

(G) Percentage of infected cells with pseudotyped SARS-CoV-2 (VSV-eGFP-SARS-CoV-2) at 24, 48 and 72 hours post infection.

(H) Staining for DAPI (nuclei, blue), GFAP (astrocytes, red) and eGFP (virus, green) in astrocytes infected with pseudotyped SARS-CoV-2 (VSV-eGFP-SARS-CoV-2) at 24, 48 and 72 hours post infection. The data represents the percentage of dsRNA-stained cells of SARS-CoV-2-S positive cells (10 fields were analyzed).

All data are representative of at least two independent experiments performed in triplicate or quadruplicate and shown as mean ± SEM. P-values were determined by two-tailed unpaired tests with Welch's correction (E) or one-way ANOVA followed by Tukey's post hoc test (F and G). **$P < 0.01$; *** $P < 0.001$; **** $P < 0.0001$ compared to the mock group.

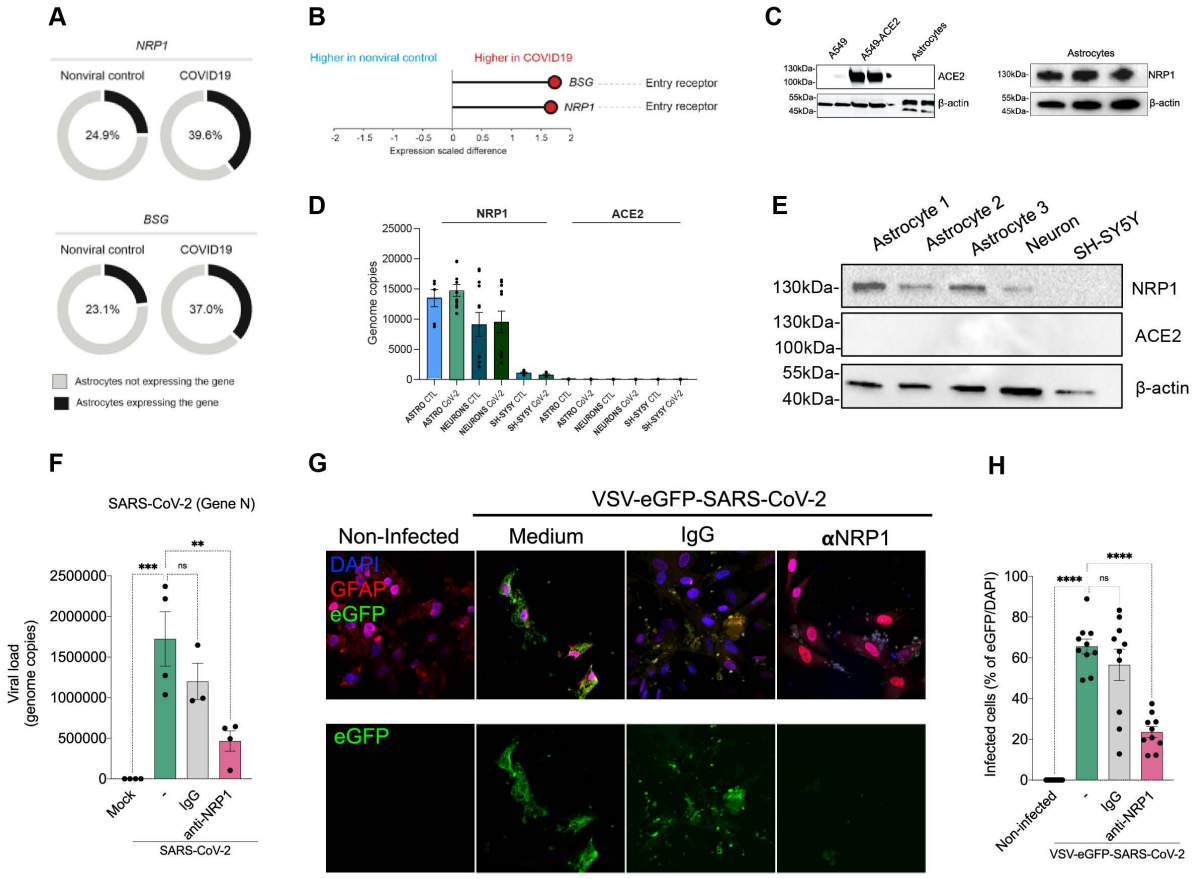

Figure 5. SARS-CoV-2 infects astrocytes via NRP1.

(A) Percentage of astrocytes expressing entry receptor genes in COVID-19 patients compared to astrocytes from non-infected controls.

(B) BSG and NRP1 are differentially expressed in astrocytes from COVID-19 patients compared to astrocytes from non-infected controls. The x-axis shows the average expression difference (scaled) between COVID-19 patients and non-infected controls.

(C) Immunoblot analyses of ACE2 and NRP1 using an extract of non-infected neural stem cell-derived astrocytes. Beta-actin was used as loading control. To control for ACE2 expression, we used A549 cells and A549 cells overexpressing ACE2.

(D) Gene expression of *NRP1* and *ACE2* in human neural stem cell-derived astrocytes, NSC-derived neurons and SH-SY5Y cells. Gene expression of NRP1 and ACE2 were evaluated by RT-PCR normalized to the expression of 18S. A serial dilution of hACE2 and NRP1 were used as a standard curve.

(E) Immunoblot analyses of NRP1 and ACE2 using an extract of non-infected neural stem cell-derived astrocytes, NSC-derived neurons and the SH-SY5Y cell line. Beta-actin was used as loading control.

(F) Neural stem cell-derived astrocytes were pre-incubated with a NRP1-neutralizing antibody and then harvested 24h post infection to measure SARS-CoV-2 viral load.

(G) Astrocytes were stained for DAPI (nuclei, blue), GFAP (astrocytes, red) and eGFP (virus, green). Cells were pre-incubated with the NRP1-neutralizing antibody and then assessed 48h post infection with the SARS-CoV-2 pseudotyped virus (VSV-eGFP-SARS-CoV-2).

(H) Percentage of infected cells. Images were acquired with 630x magnification. Scale bar indicates 50 µm. All data are representative of at least two independent experiments performed in triplicate and shown as mean ± SEM. P-values were determined by one-way ANOVA followed by Tukey's post (E and G). **$P < 0.01$; *** $P < 0.001$; **** $P < 0.0001$ compared to the mock group.

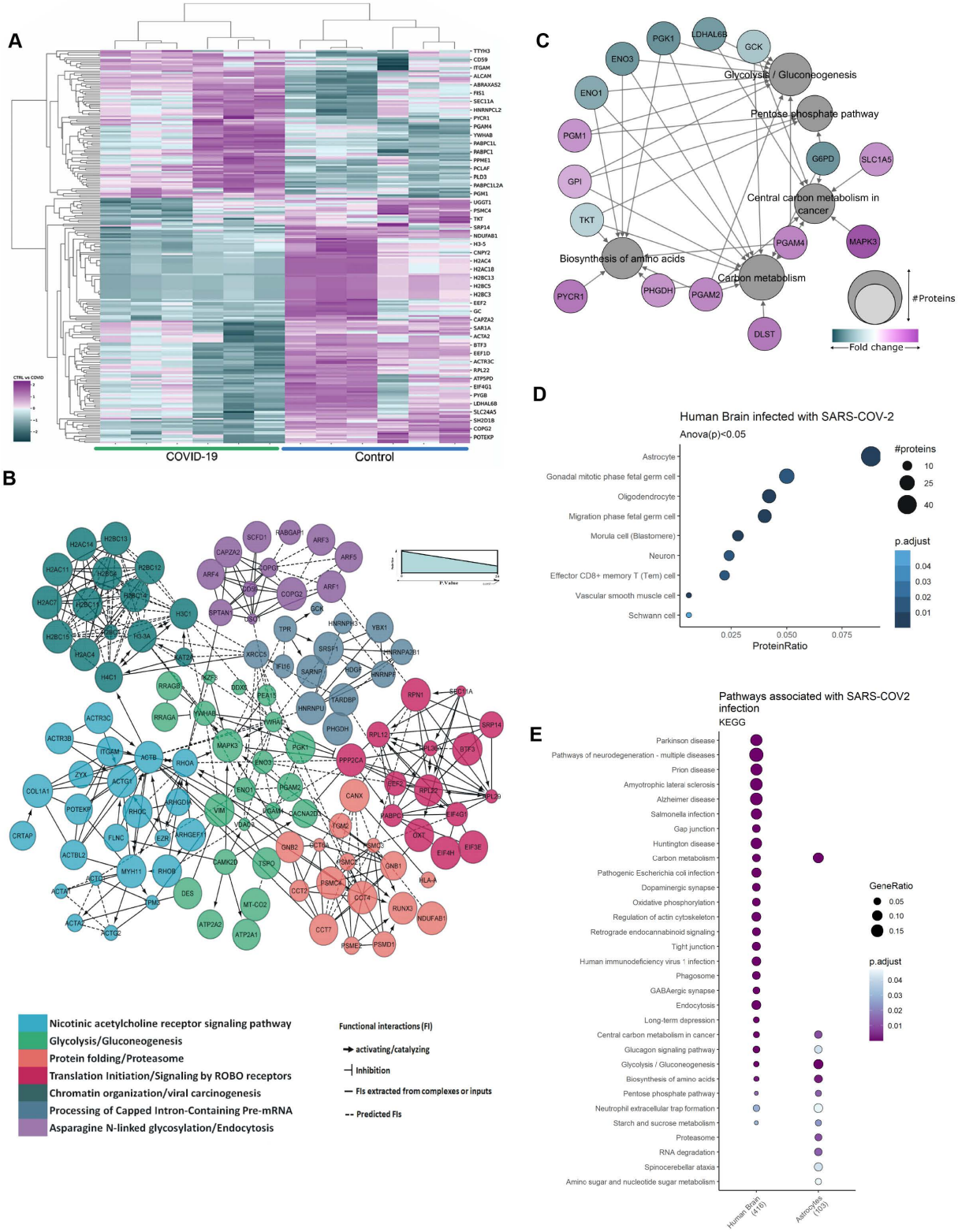
A
COVID-19
Control
B
Nicotinic acetylcholine receptor signaling pathway
Glycolysis/Gluconeogenesis
Protein folding/Proteasome
Translation Initiation/Signaling by ROBO receptors
Chromatin organization/viral carcinogenesis
Processing of Capped Intron-Containing Pre-mRNA
Asparagine N-linked glycosylation/Endocytosis
Functional interactions (FI)
activating/catalyzing
Inhibition
FIs extracted from complexes or inputs
Predicted FIs
C
Glycolysis / Gluconeogenesis
Pentose phosphate pathway
Central carbon metabolism in cancer
Biosynthesis of amino acids
Carbon metabolism
#Proteins
Fold change
D
Human Brain infected with SARS-COV-2
Anova(p)<0.05
Astrocyte
Gonadal mitotic phase fetal germ cell
Oligodendrocyte
Migration phase fetal germ cell
Morula cell (Blastomere)
Neuron
Effector CD8+ memory T (Tem) cell
Vascular smooth muscle cell
Schwann cell
ProteinRatio
#proteins
p.adjust
E
Pathways associated with SARS-COV2 infection
KEGG
Parkinson disease
Pathways of neurodegeneration - multiple diseases
Prion disease
Amyotrophic lateral sclerosis
Alzheimer disease
Salmonella infection
Gap junction
Huntington disease
Carbon metabolism
Pathogenic Escherichia coli infection
Dopaminergic synapse
Oxidative phosphorylation
Regulation of actin cytoskeleton
Retrograde endocannabinoid signaling
Tight junction
Human immunodeficiency virus 1 infection
Phagosome
GABAergic synapse
Endocytosis
Long-term depression
Central carbon metabolism in cancer
Glucagon signaling pathway
Glycolysis / Gluconeogenesis
Biosynthesis of amino acids
Pentose phosphate pathway
Neutrophil extracellular trap formation
Starch and sucrose metabolism
Proteasome
RNA degradation
Spinocerebellar ataxia
Amino sugar and nucleotide sugar metabolism
GeneRatio
p.adjust
Human Brain (410)
Astrocytes (103)

Figure 6. Proteomic changes in SARS-CoV-2-infected human astrocytes and *postmortem* brain tissue from COVID-19 patients.

(A) Hierarchical clustering of differentially expressed proteins in human neural stem cell-derived astrocytes that were infected *in vitro* with SARS-CoV-2 (MOI 0.1) for 1h, washed thoroughly and harvested after 24h. Mock infection was used as a control.

(B) Reactome functional interaction network of differentially regulated genes in human neural stem cell-derived astrocytes infected with SARS-CoV-2. Seven different colors show 7 protein clusters of enriched pathways and the line types represent protein-protein interactions and downstream activation or inhibition related to gene modulation, showing how some pathways can be affected by SARS-CoV-2 infection ($p<0.05$ calculated based on binomial test).

(C) Network of proteins found differentially regulated in SARS-COV-2-infected astrocytes and their respective pathways, enriched according to the KEGG database. The pathways are represented by gray circles and their size is proportional to the number of proteins differentially regulated; proteins are represented by the smallest circles, colored according to their fold change.

(D) Cell type enrichment analysis using the dataset generated from *postmortem* brain tissue from patients who died of COVID-19. Dot size represents the number of proteins related to the respective cell type and the color represents the p value adjusted by false discovery rate (FDR).

(E) KEGG enrichment analysis of differentially expressed proteins in SARS-CoV-2-infected astrocytes *vs*. mock as compared to *postmortem* brain tissue from COVID-19 patients *vs.* controls. Dot size represents the number of proteins related to the respective cell type and the color represents the p value adjusted by false discovery rate (FDR).

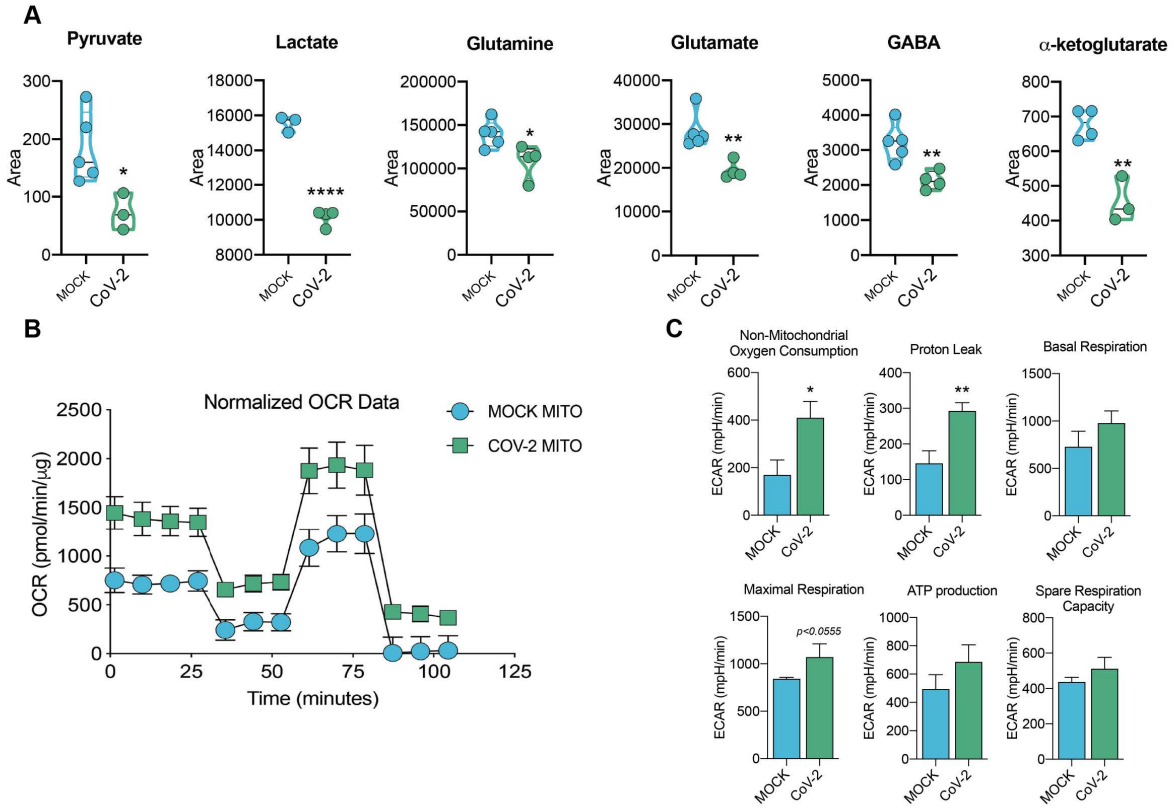

Figure 7. SARS-CoV-2 infection alters astrocyte metabolism. Human neural stem cell-derived astrocytes were infected *in vitro* with SARS-CoV-2 (MOI 0.1) for 1h, washed thoroughly and harvested after 24h. Mock infection was used as a control.

(A) High-resolution mass spectrometry quantification of pyruvate, lactate, glutamine, glutamate, GABA and α-ketoglutarate in SARS-CoV-2 infected astrocytes *vs.* mock. The integration area of each peak was used to calculate the violin plot graph and an unpaired t-test with Welch's correction was used for statistical comparison.

(B) Oxygen consumption rate (OCR) of SARS-CoV-2 infected astrocytes *vs.* mock. SeaHorse Flux Analysis using the MitoStress test where basal respiration was measured followed by determination of respiration in response to oligomycin, FCCP, and rotenone/antimycin. Data are representative of at least two independent experiments performed in triplicate (metabolomics) or

quintuplicate (SeaHorse Flux analysis), and shown as mean ± SEM. P values were determined by two-tailed unpaired t-test with Welch's correction. *P < 0.05; **P < 0.01; **** P < 0.0001 compared to mock.

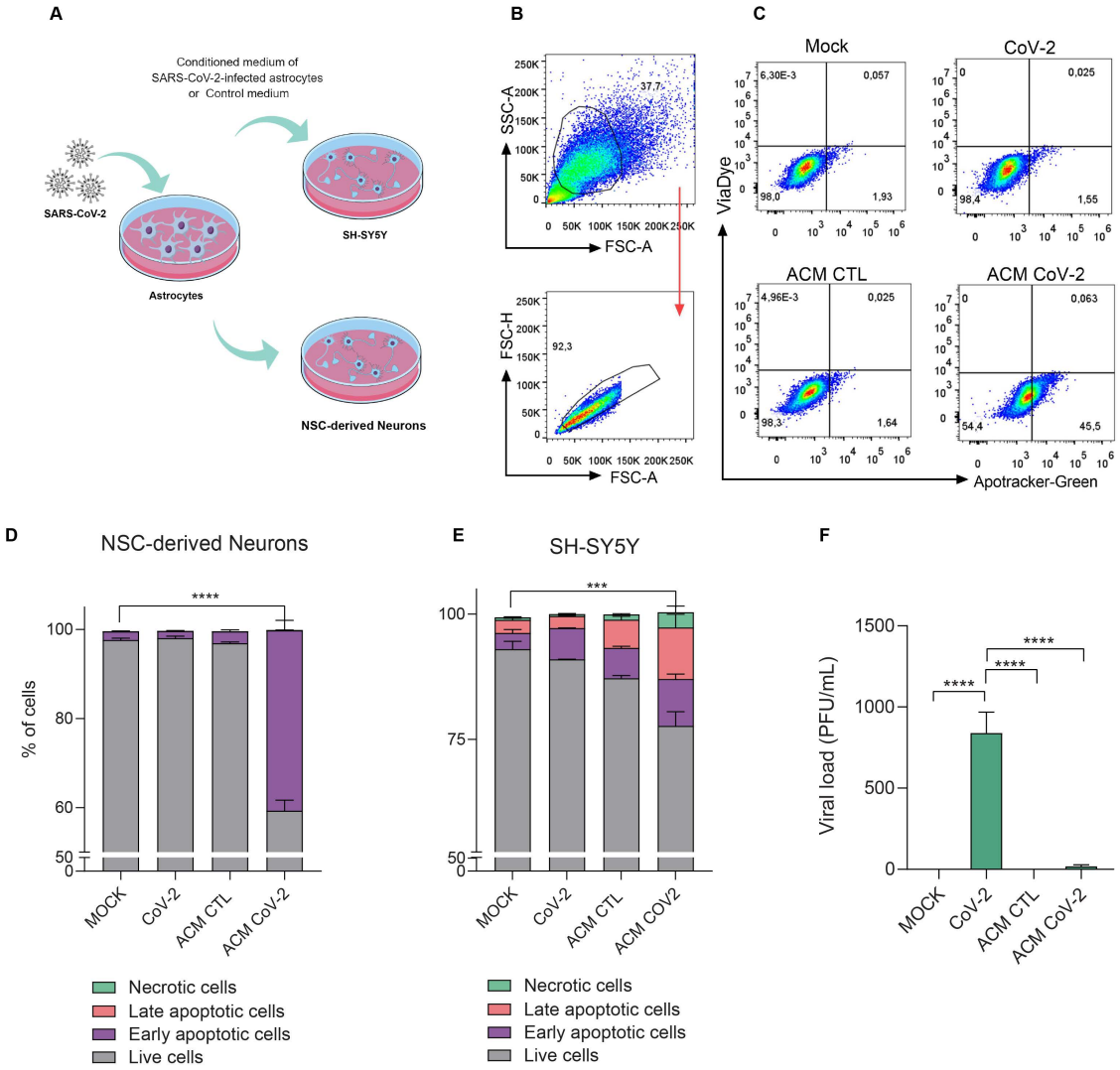

Figure 8. Medium conditioned by SARS-CoV-2-infected astrocytes reduces neuronal viability.

(A) Human NSC-derived neurons and SH-SY5Y neuronal cells were cultured for 24h in the

presence of media conditioned by uninfected astrocytes (mock infection; ACM CTL) or SARS-CoV-2-infected astrocytes (ACM CoV-2).

(B) Cellular viability as measured by apotracker/fixable viability stain (FVS) and analyzed by flow cytometry. Representative gating strategies are shown.

(C) Representative dot-plots of neuronal viability.

(D) Percentage of living or nonliving NSC-derived neurons and (E) SH-SY5Y cells. Cells were classified as living (gray bars; double-negative), in early apoptosis (purple bars; apotracker+/FVS-) in late apoptosis (pink bars; double-positive) or necrotic (green bars apotracker-/FVS+).

(F) SARS-CoV-2 viral load detection in differentiated SH-SY5Y neurons using RT-PCR. Data are representative of two independent experiments performed in triplicate, and shown as mean ± SEM. P values were determined by one-way ANOVA followed by Tukey's post hoc test. ***$P < 0.001$; ****$P < 0.0001$ compared to the mock group.

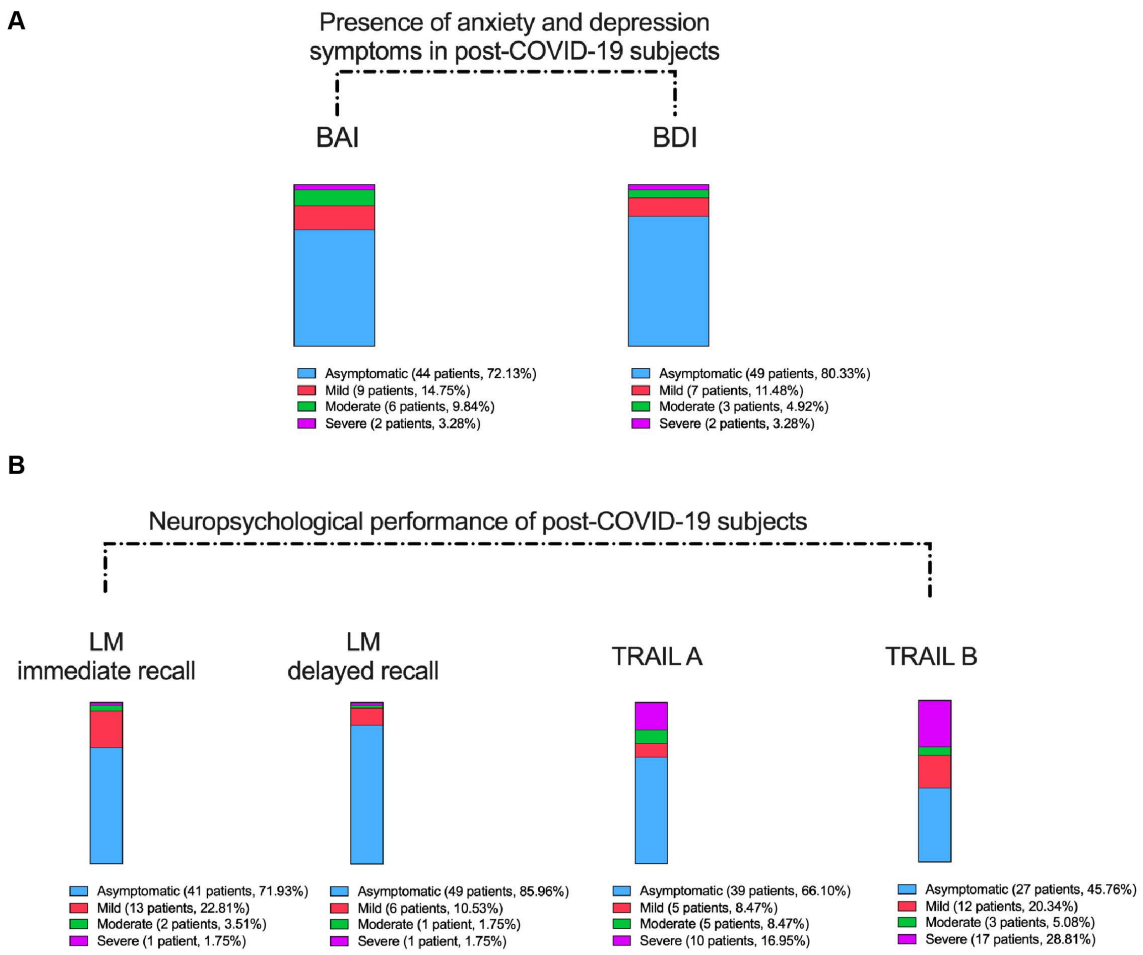

Figure S1. Frequency of neuropsychological impairment in individuals after mild infection. The subgroup of individuals who underwent neuropsychological evaluation presented a median age of 37.8 years (range 21-63 years), 16 years of education (range 6-24 years) and 59 days after COVID-19 diagnosis (range 21-120 days). The median values of BDI (Beck Depression Inventory; scale 0-36), and also of BAI (Beck Anxiety Inventory; scale 0-45) were 6 points. The median score of CFQ-11 (Chalder Fatigue Questionnaire) was 16 (scale 0-32). (A) Severity of symptoms of anxiety (BAI) and depression (BDI). (B) Severity of impairments in logical memory (LM; Wechsler Memory Scale) and cognitive function (TRAIL Making Test A and B).

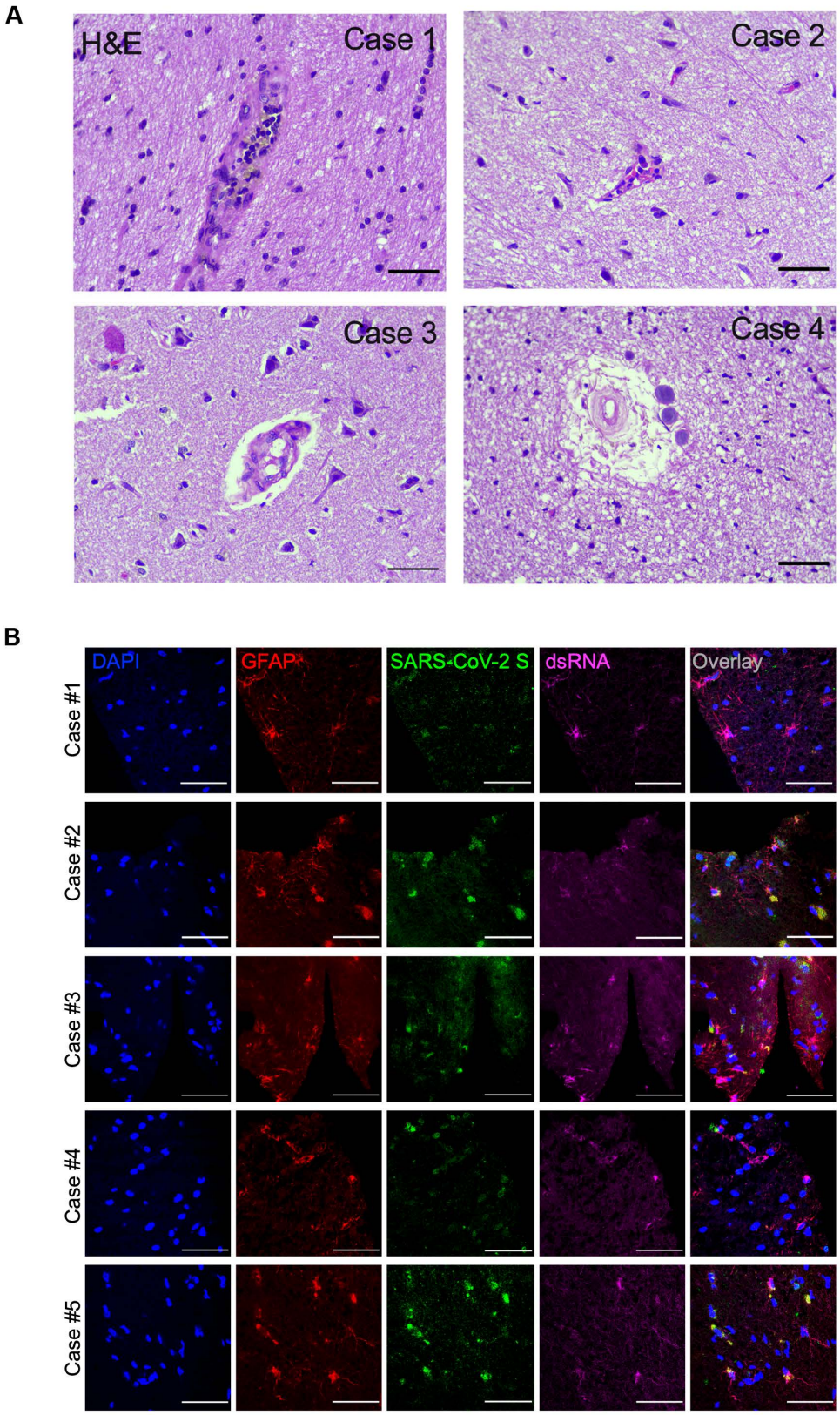
A
H&E
Case 1
Case 2
Case 3
Case 4
B
DAPI
GFAP
SARS-CoV-2 S
dsRNA
Overlay
Case #1
Case #2
Case #3
Case #4
Case #5

Figure S2. SARS-CoV-2 infects the central nervous system and replicates in astrocytes. (A) Histopathological alterations revealed by H&E images of *postmortem* brain tissue from individuals who died of COVID-19. Samples from 26 individuals were analyzed; 5 showed alterations. Case 1: intraparenchymal cerebral vessel with margination of inflammatory cells through endothelium; Case 2: focal infiltration of inflammatory cells – diapedesis; Case 3: intraparenchymal vascular damage; Case 4: perivascular edema and senile corpora amylacea. Case 5 is shown in Figure 2.

(B) Representative confocal images of the brain tissue of the 5 COVID-19 patients who manifested histopathological alterations. Staining of glial fibrillary acidic protein (GFAP, red), double-stranded RNA (dsRNA, magenta), SARS-CoV-2-S (green) and nuclei (DAPI, blue). Images were acquired with 630x magnification. Scale bar indicates 50µm.

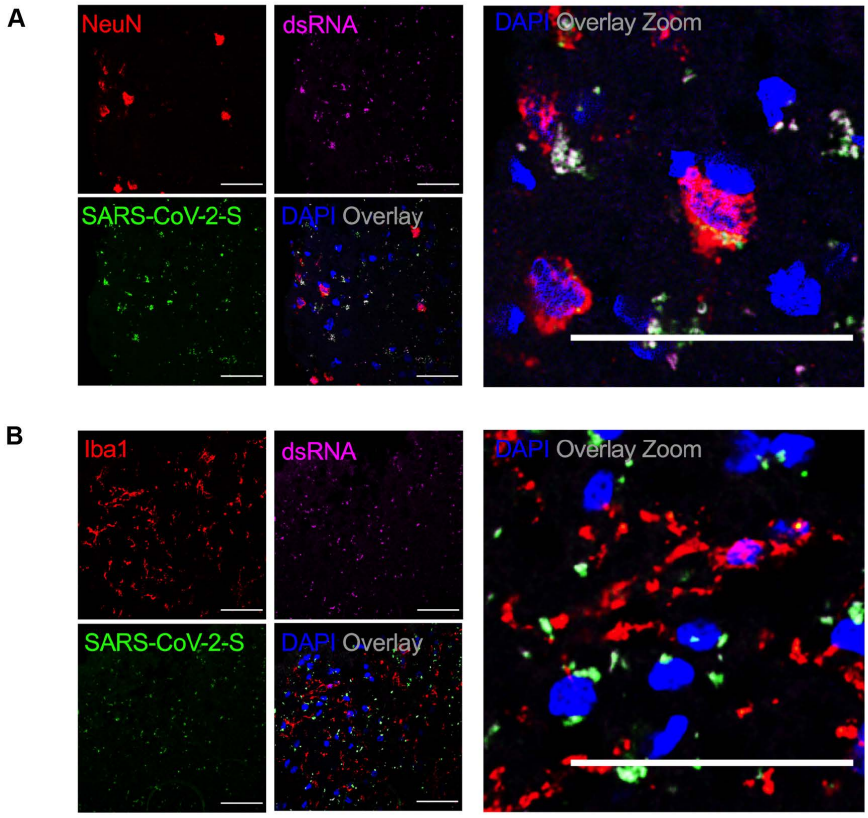

Figure S3. SARS-CoV-2 infects neurons, but not microglia, in the brains of COVID-19 patients. (A-B) Representative immunostaining and confocal analysis from brain slices from autopsies of COVID-19 patients (n=5). The image depicts staining for: (B) nuclei (DAPI, blue), NeuN (red, neuronal marker), dsRNA (magenta) and SARS-CoV-2-S (green); and (C) nuclei (DAPI, blue), ionized calcium-binding adaptor molecule 1 (Iba1, red, microglial marker), dsRNA (magenta) and SARS-CoV-2-S (green). Images were acquired with 630x magnification. Scale bar indicates 50µm.

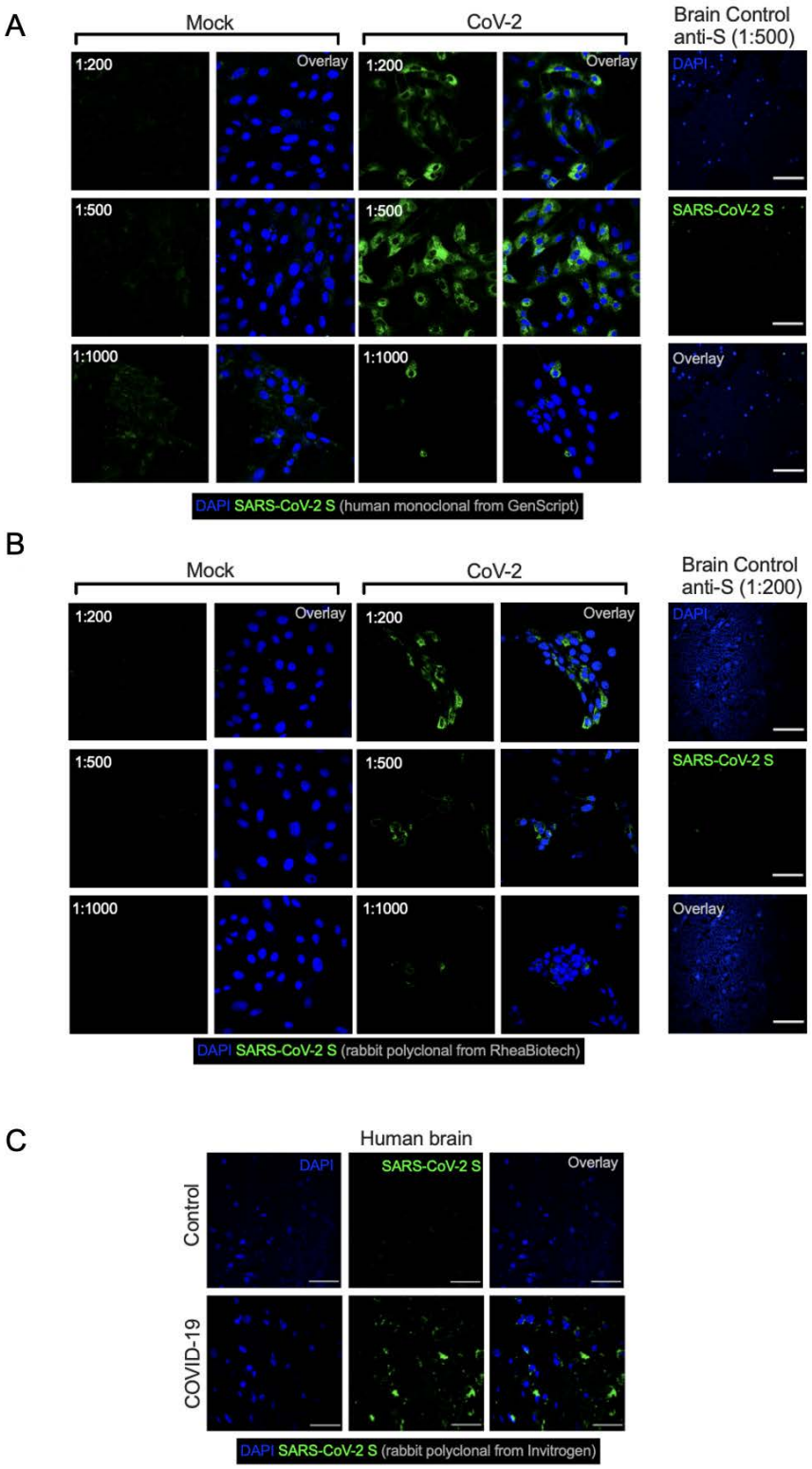

Figure S4. Validation of antibodies against SARS-CoV-2 spike (S) protein. Representative

immunostaining and confocal analysis in SARS-CoV-2-infected Vero cells and brain slices from control cases (non-COVID-19) staining with different titrations for anti-S antibodies (1:200, 1:500 and 1:1000). Immunofluorescence images show: nuclei (DAPI, blue) and (A) SARS-CoV-2-S (green, human chimeric monoclonal anti-SARS-CoV-2 spike S1, GeneScript, clone HC2001, Cat. A02038),

(B) SARS-CoV-2-S (green, rabbit polyclonal anti-SARS-CoV-2 spike, Rhea Biotech, Cat. IM-0828) or

(C) SARS-CoV-2-S (green, rabbit monoclonal anti-SARS-CoV-2 spike, clone T01KHuRb, Cat. 703959). Images were acquired with 630x magnification at the same laser intensity. Scale bar indicates 50µm.

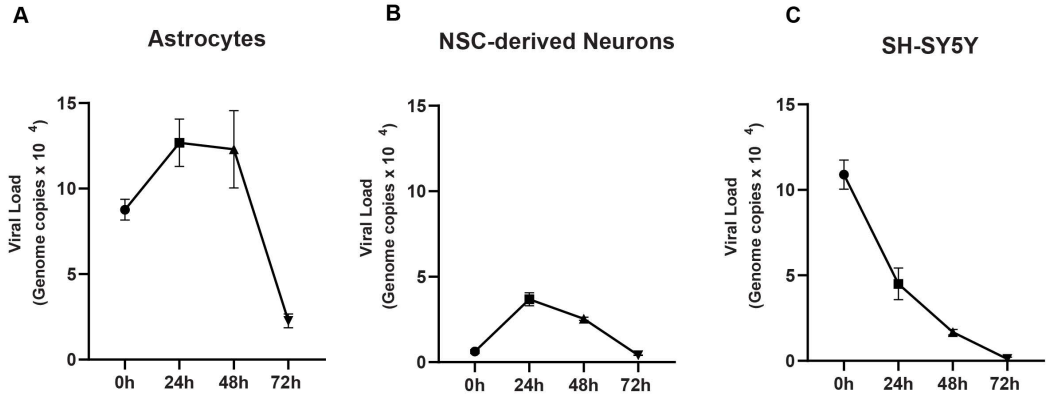

Figure S5. Viral load of Astrocytes, NSC-derived neurons and SH-SY5Y cells in vitro. The cells were infected in vitro with SARS-CoV-2 (MOI 1.0) for 1h, washed and harvested 0h, 24h, 48h and 72h after infection. SARS-CoV-2 viral load detection used RT-PCR in (A) astrocytes, (B) NSC-derived neuron and (C) SH-SY5Y neuronal cell line cell pellets. Data are

representative of two independent experiments performed in triplicate and shown as mean ± SEM.

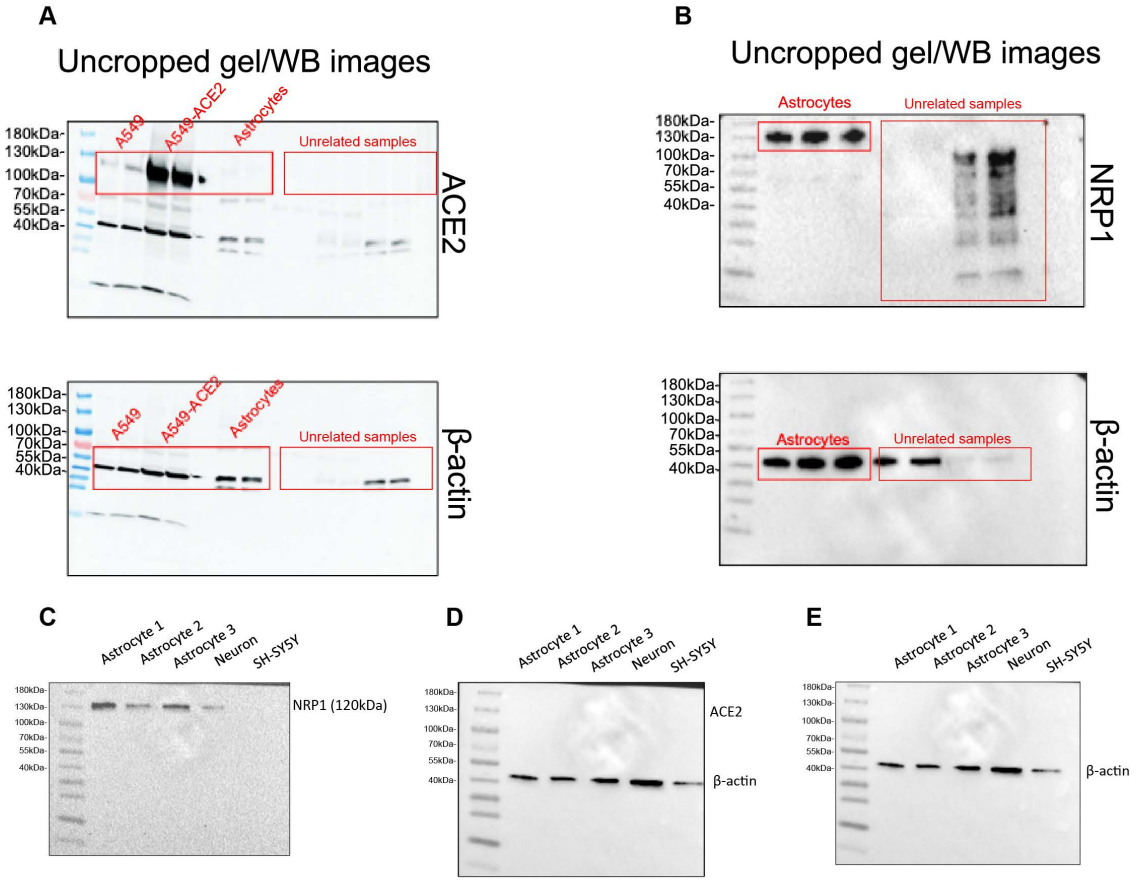

Figure S6. Full scan of the original uncropped immunoblots. (A) Original immunoblots used in Figure 5C for (A) ACE2 and β-actin, and (B) for NRP1 and β-actin.Regions of interest were cropped as indicated in red lines.

(C-E) Original immunoblots used in Figure 5E for NRP1, ACE2 a and β-actin.

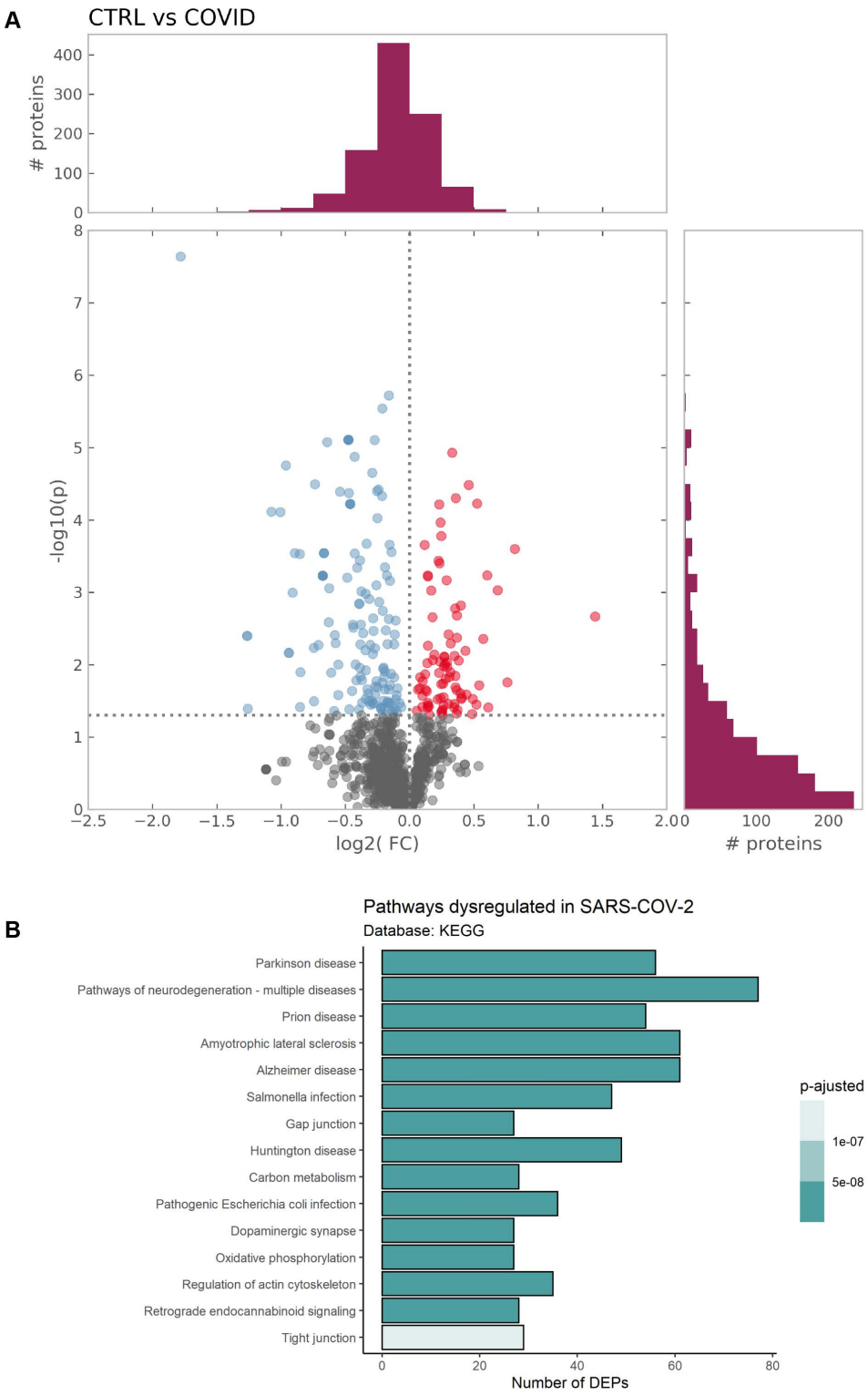

Figure S7. Proteomic analysis of SARS-CoV-2-infected astrocytes and *postmortem* brain tissue from patients who died with COVID-19.

(A) Volcano plot representing all the differentially expressed proteins found in astrocytes after SARS-CoV-2 infection.

(B) Top 15 enriched pathways by differentially expressed proteins in *postmortem* brain tissue from patients who died with COVID-19 (as per KEGG database). Dot color represents lower (blue) or higher (red) expression or no change (gray). Bar color represents the p value adjusted by the false discovery rate (FDR).

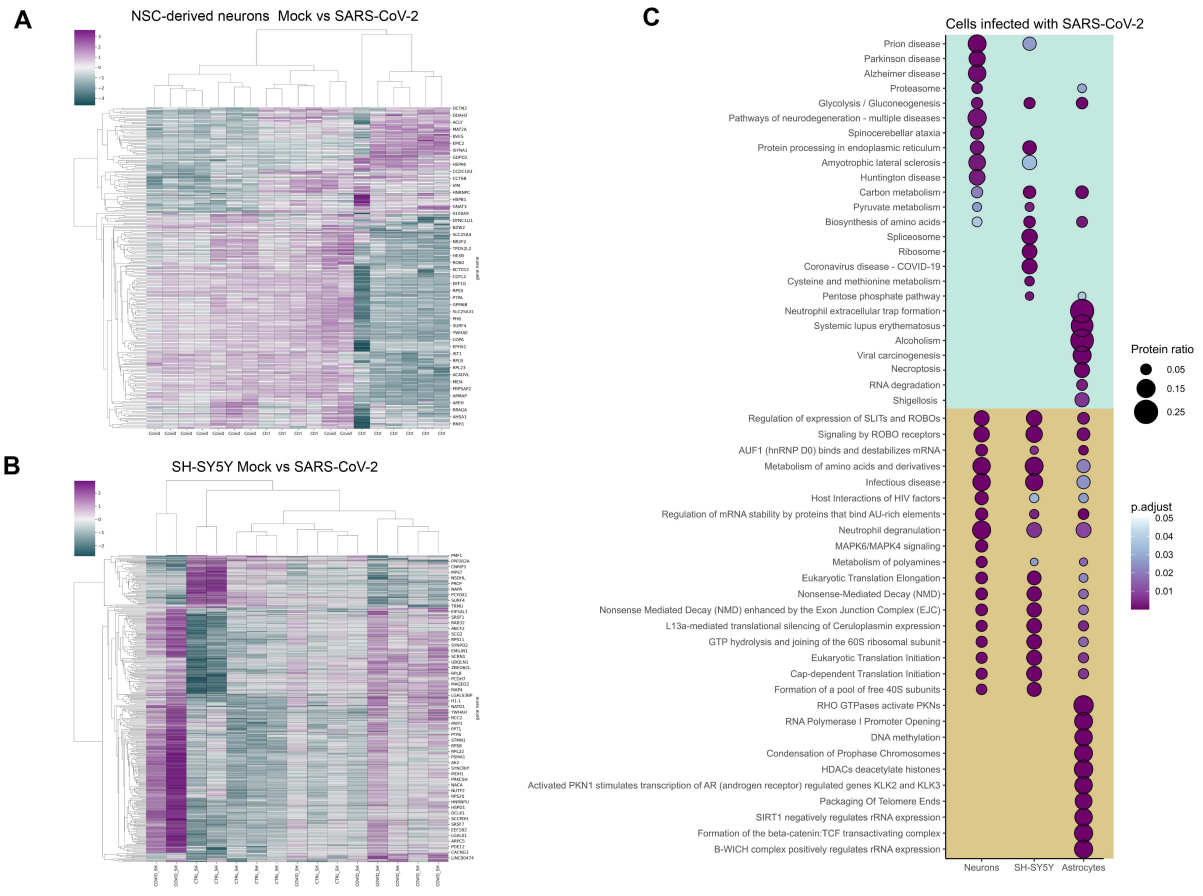

Figure S8. Proteomic analysis of SARS-CoV-2-infected NSC-derived neurons and SH-SY5Y.

(A) Hierarchical cluster analysis of the protein expression pattern in NSC-derived neurons infected with SARS-CoV-2 (MOI 0.1).

(B) Hierarchical cluster analysis of the protein expression pattern in SH-SY5Y cells infected with SARS-CoV-2 virus (MOI 0.1).

(C) Comparison of enrichment pathway analysis of all the statistically deregulated proteins from SARS-CoV-2 infections between NSC-derived Astrocytes, NSC-derived Neurons and SH-SY5Y cells.

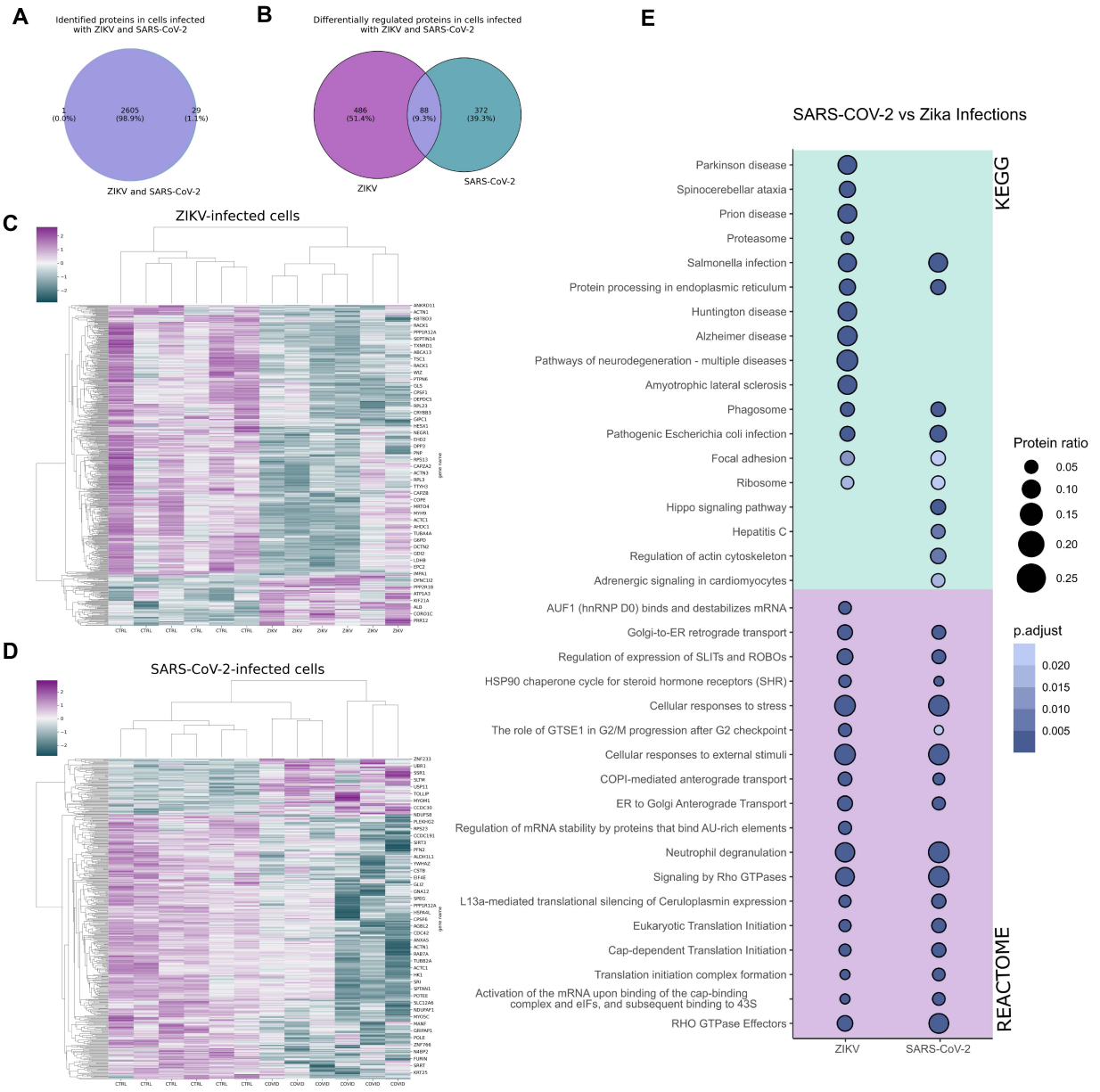

Figure S9. (A) Venn diagram of all proteins identified by Progenesis QI for Proteomics using the Homo sapiens data bank (UNIPROT - UP000189706) and 1% FDR after NSC-derived astrocyte infection with SARS-CoV-2 and ZIKV.

(B) Venn diagram of all proteins found significantly deregulated by label-free analysis between SARS-CoV-2 and ZIKV.

(C) Hierarchical cluster analysis of the protein expression pattern in NSC-derived astrocytes

infected with ZIKV (MOI 1.0).

(D) Hierarchical cluster analysis of the protein expression pattern in NSC-derived astrocytes infected with SARS-CoV-2 virus (MOI 1.0).

(E) Enrichment pathway analysis of all the statistically deregulated proteins from SARS-CoV-2 and ZIKV infections.

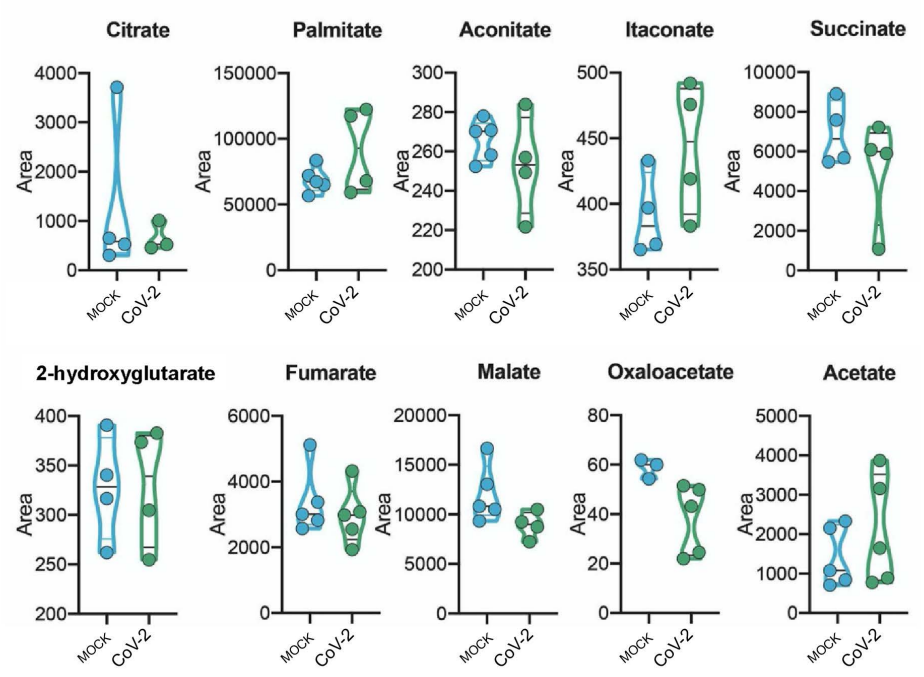

Figure S10. Metabolomic analysis of SARS-CoV-2-infected astrocytes. Human neural stem cell-derived astrocytes were infected *in vitro* with SARS-CoV-2 (MOI 0.1) for 1h, washed thoroughly and harvested after 24h. Mock infection was used as a control. High-resolution mass spectrometry quantification of citrate, palmitate, aconitate, itaconate, succinate, 2-hydroxyglutarate, fumarate, malate, oxaloacetate and acetate in SARS-CoV-2 infected astrocytes *vs.* mock. The integration area of each peak was used to calculate the violin plot graph and an unpaired t-test with Welch's correction was used for statistical comparison.

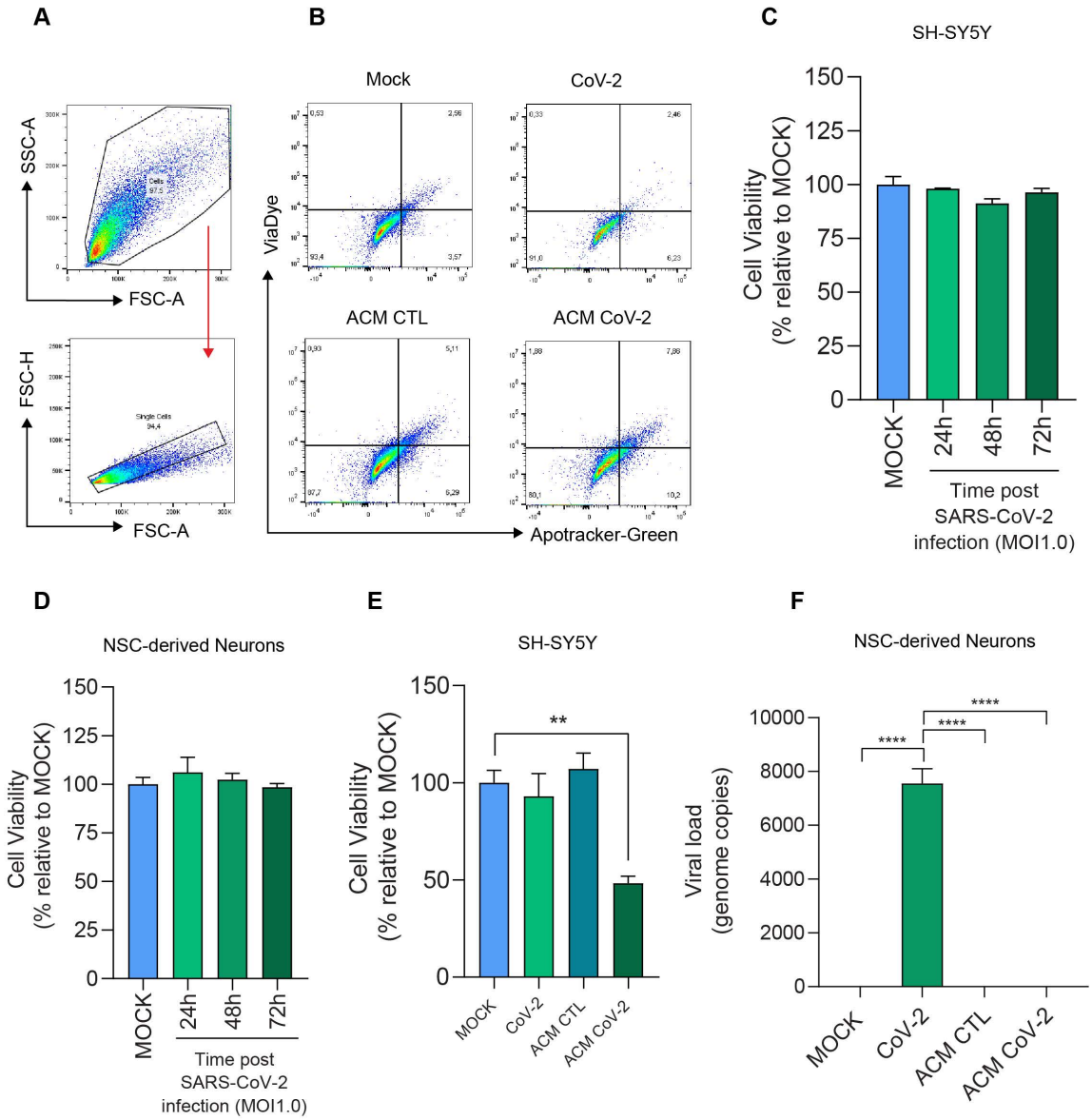

Figure S11. Medium conditioned by SARS-CoV-2-infected astrocytes reduces neuronal viability despite no change from direct virus exposure to neurons. Differentiated SH-SY5Y cells were cultured for 24h in the presence of medium conditioned by SARS-CoV-2-infected astrocytes (ACM CoV-2) or uninfected astrocytes (ACM CTL). Cellular viability was measured by apotracker/fixable viability stain (FVS) and analyzed by flow cytometry.

(A) Representative gating strategies.

(B) Representative dot-plots of neuronal viability.

(C) NSC-derived neuron and (D) SH-SY5Y neuronal cell viability upon SARS-CoV-2 infection. The cells were infected *in vitro* with SARS-CoV-2 (MOI 1.0) for 1h, washed thoroughly and harvested after 24h. Mock infection was used as a control. The NSC-derived neurons were assessed using a ATP-quantifying, luminescence-based cell viability assay (CellTiter-Glo) at 24h, 48h and 72h post infection. SH-SY5Y viability was assessed using calcein AM staining (Invitrogen) at 24, 48 and 72 hours post infection.

(E) Differentiated SH-SY5Y cells were cultured for 24h in the presence of medium conditioned by SARS-CoV-2-infected astrocytes (ACM CoV-2) or uninfected astrocytes (ACM CTL).

(F) SH-SY5Y neuronal cell line and (G) NSC-derived neurons were exposed for 24h to media conditioned by astrocytes for 24h, 48h and 72h. Cellular viability was measured by apotracker/fixable viability stain (FVS) and analyzed by flow cytometry. Representative graph of percentage of live cells represents the double-negative population of (F) SH-SY5Y cells and (G) NSC-derived neurons. Data are representative of two independent experiments performed in triplicate (A,B,F,G) or quintuplicate (C,D,E) and shown as mean ± SEM. P values were determined by one-way ANOVA followed by Tukey's post hoc test. *$P < 0.05$; **$P < 0.01$; ***$P < 0.001$ compared to the mock group.

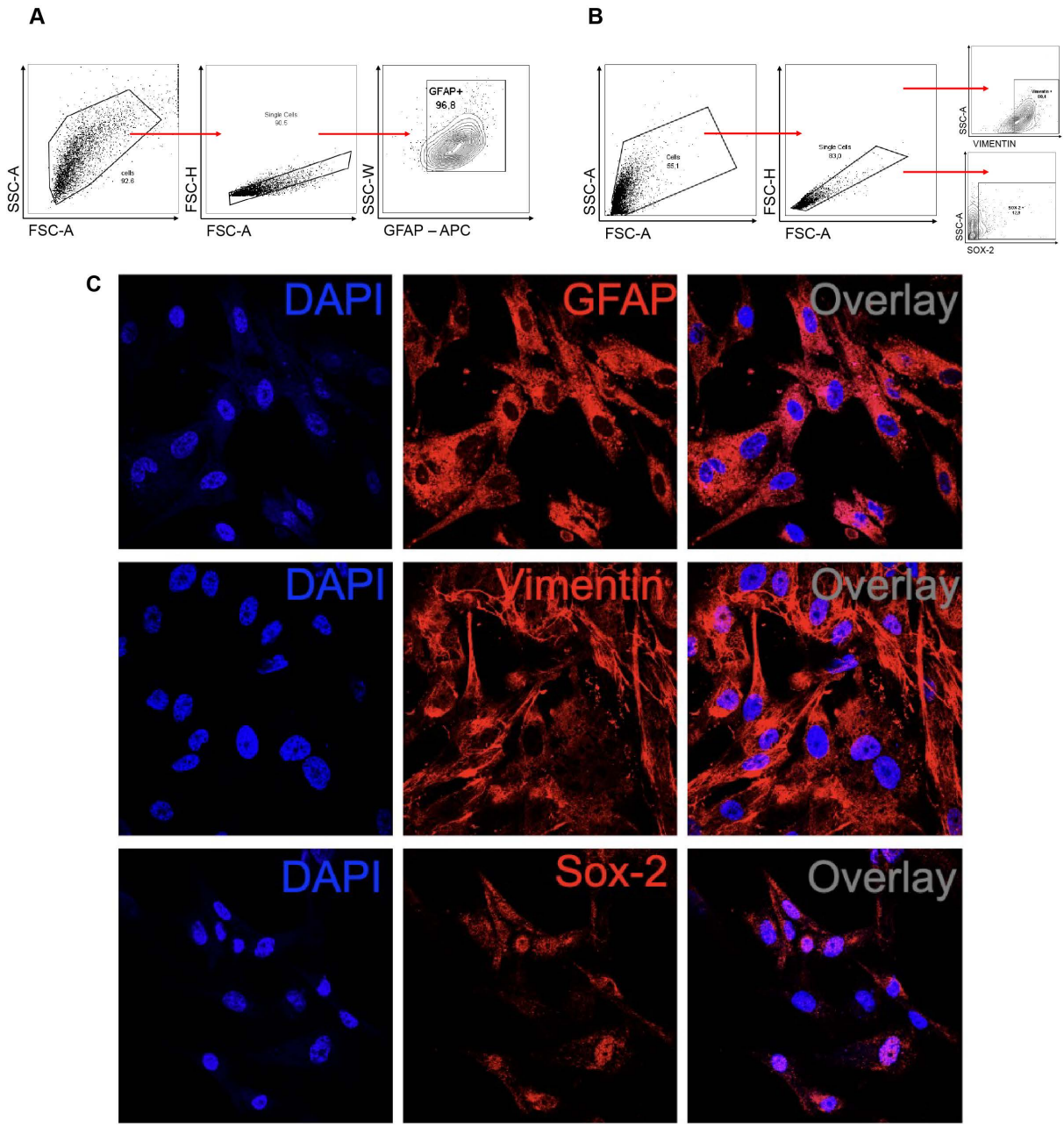

Figure S12. Characterization of human astrocyte cultures. Cells were trypsinized for FACS analysis and incubated with antibodies against GFAP, vimentin and SOX-2.

(A) Cells were analyzed and the results were plotted as SSC-A *vs.* GFAP (APC). The percentage of positive cells is indicated in the representative contour plot.

(B) Cells were analyzed and the results were plotted as SSC-A *vs.* SOX-2 (APC) and SSC-A *vs.*

vimentin (BB515). The percentage of positive cells is indicated in the representative contour plot.

(C) Staining for GFAP, vimentin, SOX-2 (red) and nuclei (DAPI, blue). Images were acquired with 630x magnification. Scale bar indicates 50µm.

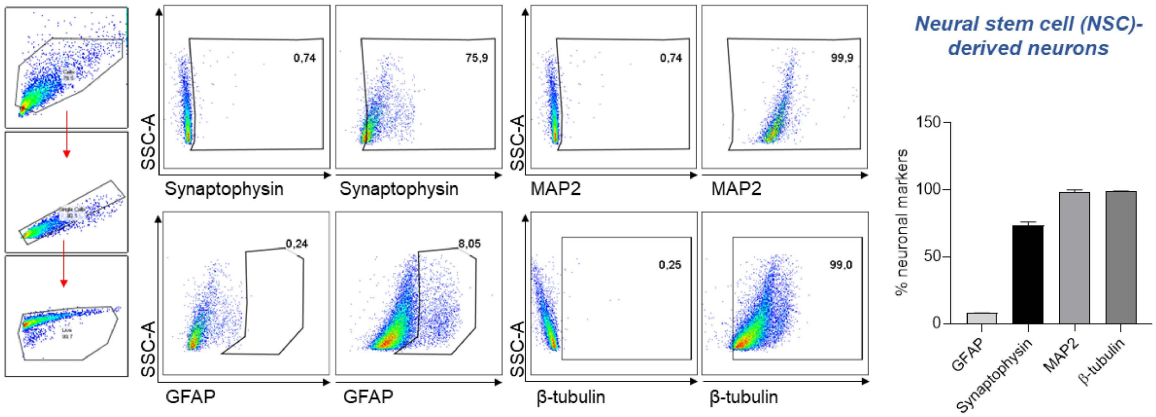

Figure S13. Characterization of human neural stem cell-derived neurons. The cells were trypsinized for FACS analysis and incubated with antibodies against synaptophysin, MAP2, GFAP and β-tubulin. Cells were analyzed and the results were plotted as SSC-A *vs.* synaptophysin, MAP2, GFAP or β-tubulin. The percentage of positive cells is indicated in the representative contour plot.